BIPROPELLANT ENGINE PLUME STUDY[†]

H. E. Scott and D. F. Frazine
Arnold Engineering Development Center
Arnold Air Force Station, Tennessee

and

Lt E. G. Lund
Air Force Rocket Propulsion Laboratory
Edwards Air Force Base, California

ABSTRACT

Data from the first phase of an experimental program to characterize the exhaust properties of a liquid bipropellant engine under vacuum conditions are presented and discussed. Emphasis is placed on measurements of the mass flux in the plume backflow region of a 5 lb_f bipropellant thruster at angles up to 150° with respect to the plume centerline using temperature compensated quartz crystal microbalances (QCMs). The measurements were conducted in a high vacuum cryogenic chamber at AEDC. The addition of new GHe and LHe cryopanels provided a blank-off pressure in the 10^{-7} torr range and maintained the background pressure in the 10^{-5} torr range while pulse firing the motor (25-100 msec pulse width, 1-10% duty cycle). Chamber recovery time was a few tenths of a second.

Several engine configurations were tested at different operating conditions so as to characterize exhaust properties and to investigate potential contamination effects. Variations included: injector--0° and 45° splash plate; combustion chamber--2 inch cylindrical, 1.5 inch cylindrical, and 2 inch conical; nozzle area ratio--50:1 and 100:1; O/F-- 1.4, 1.6, and 1.8; chamber pressure--75, 100, and 125 psia; pulse duty cycle--1%, 5%, 10%, and continuous.

QCM data for the plume mass flux at 25° to 150° from the plume centerline are presented. Comparisons with plume models demonstrate the importance of treating the nozzle boundary layer expansion into the plume backflow region. These data are the only known data describing the boundary layer expansion of a hot rocket engine exhaust into a hard vacuum representative of space conditions. In addition to the QCMs, other diagnostic measurements were made to characterize the exhaust properties during the first phase of this experimental study. Some of these results are presented in a companion paper. During the second phase of testing electron beam fluorescence, mass spectrometric, additional QCM and scattering measurements will be performed.

1.0 INTRODUCTION

The potential contamination of spacecraft surfaces and components by exhaust products from space thrusters, whether solid, liquid or electric, has received increased attention from the spacecraft design community in recent years[1-6]. This concern is attributed to the development of more sophisticated spacecraft systems designed to perform multiple, non-interferring missions for longer periods of time in space. Contamination and subsequent degradation of sensitive spacecraft surfaces and components, such as thermal control coatings, solar cells, antennas, optical devices, and especially cooled infrared sensors, can compromise mission objectives and lead to a reduction in spacecraft lifetime. For example, contamination of thermal control surfaces with low absorptivity-to-emissivity properties, required for passive control of spacecraft temperatures, can cause an increase in spacecraft temperature, thus affecting the spacecraft mission and/or lifetime.

In order to predict the effects of rocket exhaust plumes from liquid bipropellant and monopropellant engines on spacecraft surfaces of interest, a computer code (CONTAM)[7] was developed by McDonnell Douglas Corporation for the Air Force Rocket Propulsion Laboratory (AFRPL). Davis and Wax[8] conducted a partial verification of this code against monopropellant hydrazine data[9, 10] collected at the Jet Propulsion Laboratory (JPL). Their studies identified serious deficiencies in the code's treatment of the nozzle and plume expansion, particularly at large angles from the plume centerline. An additional deficiency in the CONTAM code, which has long been recognized, is the absence of a nozzle boundary layer treatment and subsequent boundary layer

expansion into the plume backflow region (i.e., expansion angles greater than 90 degrees). Proper treatment of boundary layer processes is critical to the successful prediction of plume contamination effects since most spacecraft surfaces are located in the plume backflow region. Consequently, the AFRPL has initiated studies to improve the CONTAM code by correcting these deficiencies. An extensive plume data base for a monopropellant hydrazine thruster, along with cold flow and condensation data for pure and mixed gas expansions[12, 13], has been obtained at the AEDC[11] and JPL[9]. The purpose of the present program is to provide a quantitative data base for a representative bipropellant engine for further verification of the improved code.

Prior to this experimental study very little bipropellant plume data existed[14], and most of these data were qualitative. As a result of the development of improved in situ measurement techniques[16, 17], as well as a high performance 5 lb_f bipropellant engine[15] small enough to test in a vacuum chamber under space simulation conditions, the subject measurements program was initiated at the Air Force Arnold Engineering Development Center (AEDC). The 5 lb_f thruster was fired in a space simulation chamber which had been suitably modified to provide the necessary cryogenic pumping capability, and various in situ measurements were performed. Here, we are reporting the results from the first phase of this experimental program.

The basic objectives of the program can be summarized as follows:

(1) demonstrate a cryogenic pumping capability sufficient to permit mass flux measurements in the backflow region of a 5 lb_f bipropellant engine;

(2) measure the mass flux distribution in the bipropellant plume over a wide range of angles with respect to the nozzle axis for CONTAM code verification; vary the engine configuration and operating conditions to determine any significant dependence on these parameters;

(3) fully characterize the engine by identifying all products (gaseous species, droplets, or particles) in the plume and by measurement of nozzle exit plane concentration and temperature profiles.

This paper provides an overview of the entire program and a detailed examination of the mass flux measurements. It includes discussions on the cryogenic chamber, diagnostic techniques, quartz crystal microbalance[9, 10, 18] (QCM) design and operation, and results of the mass flux measurements. Time and space limitations preclude a comprehensive discussion of all the results, although a companion paper[19] presents preliminary results of the condensed phase IR transmission measurements. A technical report describing the project in more detail will be published by AEDC in late 1978.

2.0 OVERVIEW OF THE EXPERIMENT

2.1 Cryogenic Chamber

The space simulation facility (Fig. 1) used for this study is a conventional cylindrical chamber 10 ft in diameter and 20 ft long. It is fully lined with liquid nitrogen (80°K) and refrigerated gaseous helium (20°K) cryogenic panels. Additional liquid helium cryopumps were installed both downstream and forward of the engine to pump H_2, a major constituent in the bipropellant exhaust plume.

The requirements which determine chamber performance criteria and design goals in a plume measurements program of this nature are frequently obvious but also difficult to quantify. Keep in mind the objective was to measure the mass flux distribution from the rocket engine and in this case to measure mass flux levels in the plume backflow region which are at least six orders of magnitude lower (unknown at the outset) than in the forward flow direction. Clearly the chamber background pressure must be kept sufficiently low that the plume shape is not significantly different than in an operational space environment. A careful flow field analysis is required to translate this statement into design criteria, yet no verified flow field model exists for the backflow region. A second requirement which is more easily converted into a design goal is simply a mean free path long enough to permit molecules to travel the distance from the nozzle to the QCMs with no intermolecular collisions. Mean free path calculations indicated a background pressure on the order of 10^{-5} torr or lower was needed. Hence the design goal adopted here was a chamber pressure of 1×10^{-5} torr under continuous firing of the 5 lb_f thruster for a period of 1 sec.

LHe Supply Dewar

LN₂ Liner

GHe Pump

LHe Pump

LN₂ "V" Shield

GHe Pump

QCM

LHe Pump
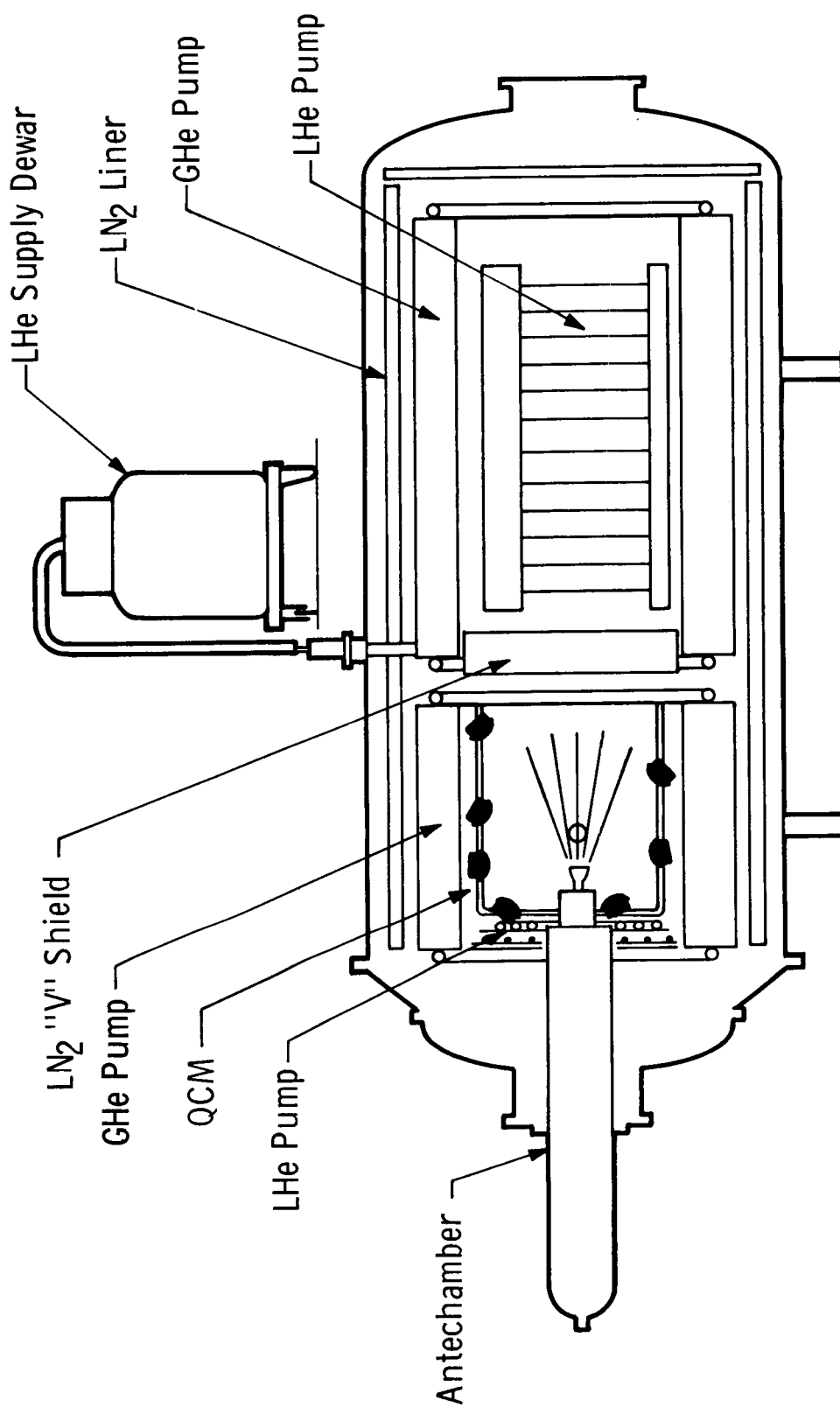
Antechamber

AEDC 10V CRYOGENIC CHAMBER

FIG. 1

687

The data presented here gives clear evidence that the chamber performed adequately for the backflow measurements. Typically during the engine firing the pressure in the backflow region, as measured by an ion gauge pointed toward the plume, was 3×10^{-5} torr. Between firings the chamber recovered quickly (in less than 0.1 sec) to a pressure of $4-8 \times 10^{-6}$ torr. To further verify that the chamber background pressure had no measurable systematic effect on the QCM data, helium was added to raise the chamber pressure to 10^{-3} torr where the effect on the QCM measurements was apparent. The details of this experiment are presented later with the QCM results.

One additional feature of the facility deserving mention is the antechamber (Fig. 1). It permitted the thruster to be withdrawn for changes in the configuration or maintenance without cycling the main chamber. This was a very practical capability since cycling the chamber required at least 24 hours.

For additional details on the chamber and its cryogenic pumping capabilities, refer to the AEDC Facility Handbook[20].

2.2 Bipropellant Engine (5 lb_f)

As mentioned earlier the thruster chosen for this study was a 5 lb_f bipropellant (MMH/N_2O_4) engine developed by Aerojet Liquid Rocket Company under an AFRPL contract[15] in 1973; specifications[21] are provided in Table 1. The thruster was installed, free to radiate, in one end of the vacuum chamber as shown in Figs. 1 and 2. It was mounted on a traversing mechanism with flexible propellant lines permitting axial translation along the chamber centerline and withdrawal into the antechamber. Effort was made, in designing the mounting arrangement, to minimize the obstruction in the plume backflow region for the QCM measurements at large angles from the nozzle axis.

TABLE 1

BIPROPELLANT ENGINE SPECIFICATIONS

Thrust (Vacuum), lb_f	5 max.
Propellants, O/F	N_2O_4/MMH
Mixture Ratio, O/F	1.4-1.8
Chamber Length, in.	1.5-2.0
Chamber Pressure, psia	75-150
Area Throat, in.^{2}	0.0186
Nozzle Area Ratio, A_e/A_t	50 and 100, Contoured
Injector	6-Element Splash Plate
Propellant Flow Rate, lb/sec	0.0167 (Nominal)
Inlet Pressure Oxidizer, psia	100-300
Inlet Pressure Fuel, psia	100-300
Dribble Volume, in.^{3}	0.0006
Nozzle/Chamber Material	Silicide-Coated, Columbium Alloy
Application	Space Propulsion/RCS Buried/Free to Radiate
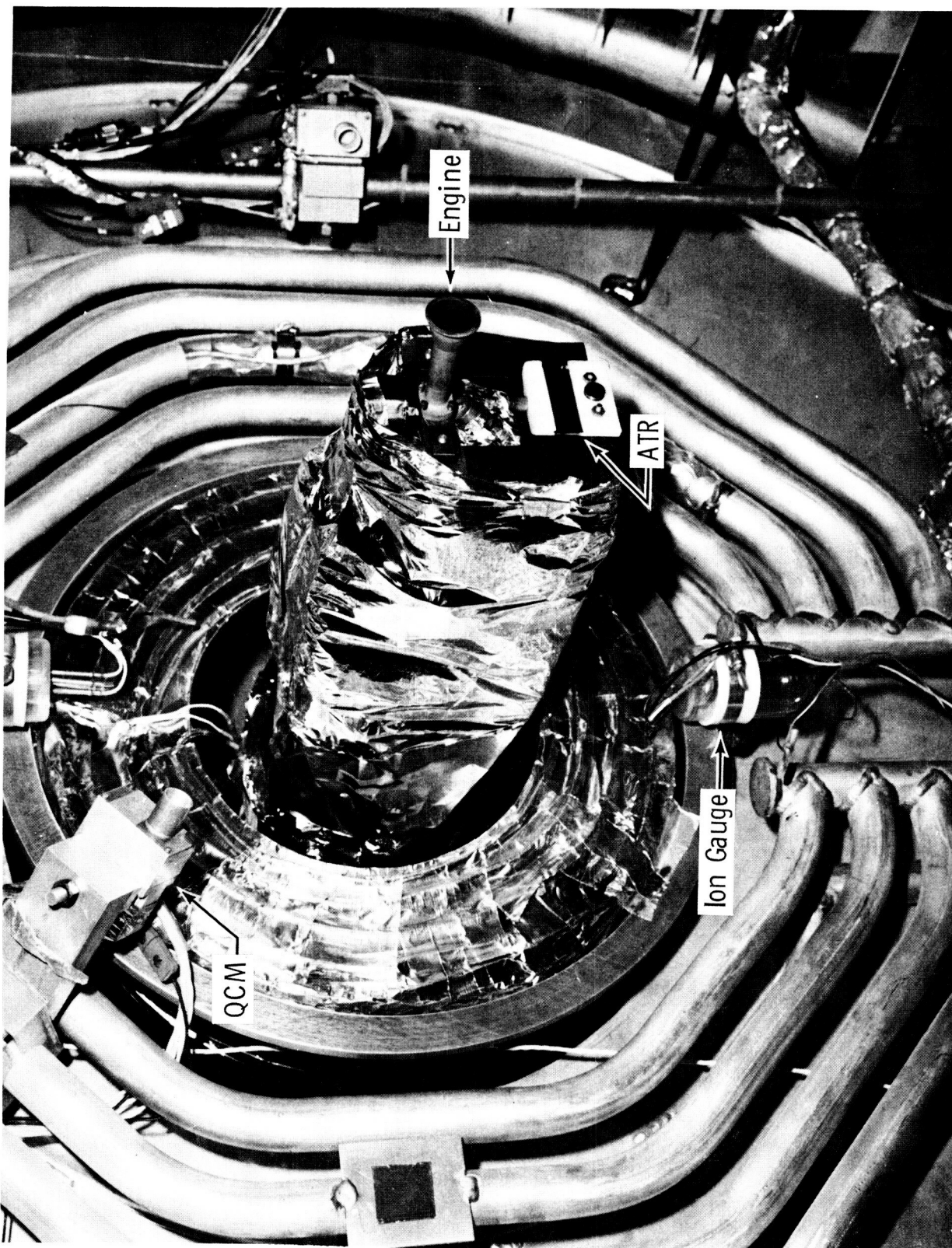
BIPROPELLANT ENGINE (5 lbf) INSTALLED IN CRYOGENIC CHAMBER. QCMs, ION GAUGES, AND ATR CRYSTAL ARE INCLUDED IN BACKGROUND.

FIG. 2

690

A variety of five thruster configurations, listed in Table 2, were tested. The five configurations were assembled from two injectors and four interchangeable combustion chamber/nozzle combinations.

2.3 Test Rationale

Although this project falls loosely into the area of plume contamination, we are not dealing with contaminants as defined in the usual literal sense. The objective was to measure the mass flux distribution in the bipropellant exhaust plume over a wide range of angles and engine operating conditions. Therefore it must remain clear throughout this paper that we are concerned with mass flux measurements even if we loosely refer to the mass flux in the plume backflow region as contamination.

The QCMs used to measure the mass flux distribution had to operate at a very low temperature in order to collect (cryopump) as many bipropellant plume constituents as possible. By operating the QCMs at 25°K, based on known equilibrium vapor pressure curves[22], we could expect to cryopump all bipropellant exhaust species except H_2. The species actually collected at various QCM operating temperatures will be discussed later with the results.

TABLE 2

ENGINE CONFIGURATIONS

Config. Code	Combustion Chamber Length/Shape	Nozzle Area Ratio, A_e/A_t	Injector Splash Plate	Firing Dates
C	2 inch/cyl.	50	45 deg	Oct 5
A	1.5 inch/cyl.	50	0 deg	Oct 17-19
BL	2 inch/cyl.	100	45 deg	Nov 8-11
B	1.5 inch/cyl.	50	45 deg	Nov 21-23
D	2 inch/conical	50	45 deg	Dec 6

Another important aspect of the approach was a deliberate effort to take advantage of all available non-interference type[11, 16, 17] diagnostic methods rather than relying solely on one tool such as the QCM which would compromise the entire program if any problems were encountered. Each diagnostic technique was selected for a specific purpose and also to complement the other techniques. The best example of the latter is the manner in which the QCM, the condensed phase IR transmission, and the laser interference techniques combined to provide information which none in and by itself could produce. The two-angle laser interference technique measured the thickness of a thin film of condensed exhaust products pumped onto a cryogenically cooled optical substrate (shown in Fig. 3). When the thickness is combined with the mass of the cryodeposit measured by a QCM at the same temperature as the optical substrate, the cryodeposit density is obtained; this is a useful piece of information for identifying the constituents in the deposit. The condensed phase IR transmission[19] coupled with the laser thickness measurement yielded the optical properties[16] (n, index of refraction and k, absorption index) of the deposit. Finally, the IR transmission spectra permitted identification of all IR active species collected by the QCMs at a given temperature and helped to establish the QCM operating temperatures required to selectively collect the plume constituents. Together the three techniques provided significantly more information than the three working independently.

2.4 Measurements

The program was divided into two phases. Phase I was completed recently and is the subject of this paper; it addressed objectives 1 and 2 listed earlier.

QCMs, SOLAR CELLS, AND GERMANIUM SUBSTRATE INSTALLED IN CRYOGENIC CHAMBER.

FIG. 3

QCMs INSTALLED IN CRYOGENIC CHAMBER. AT THE EXTREME RIGHT 10 SOLAR CELLS ARE MOUNTED IN A CIRCULAR PATTERN. THE GERMANIUM SUBSTRATE FOR THE IR TRANSMITTANCE MEASUREMENT IS SHOWN NEAR THE CENTER OF THE FRAME. NOTICE THE QCM LOCATED DIRECTLY BELOW THE GERMANIUM SUBSTRATE.

Until the thruster firings began, the actual chamber performance, especially in the plume backflow region, was still unknown, making it necessary to devote some of the Phase I measurements to assessing chamber performance. As shown in Figs. 2 and 3 ion gauges were distributed throughout the backflow region for this purpose. The gauge located at the left side of Fig. 3 was attached to a mechanical vacuum feed-through which allowed it to be rotated or translated parallel to the plume axis. In addition, a mass spectrometer was used to sample and analyze the residual gases in the backflow region.

Phase I plume diagnostic instrumentation included:

a. eleven temperature-compensated quartz crystal microbalances located at angles of 25 to 150 degrees from the plume centerline to measure the mass flux distribution; see Figs. 1 - 5.

b. IR transmission of condensed exhaust products collected on a cooled optical substrate (germanium) to provide in situ identification of species deposited on the QCMs and to determine the optical properties[16] (n, k) of the condensed exhaust gases. The germanium substrate for the IR transmission measurement is shown near the center of Fig. 3. The QCM found directly below the substrate was kept at the same temperature and used in conjunction with the IR and laser interference measurements[19] in the fashion described earlier to obtain the deposit density and the optimum QCM operating temperatures.

c. two-angle laser interference to measure the thickness and the index of refraction at 0.6328 micron of the condensed exhaust gases. The laser beams were incident on the center of the same optical substrate used for the IR transmission measurement and thus provided properties for the same deposit.

Witness Plates

QCM

QCM MOUNTED ON GHe CRYOGENIC LINE. WITNESS PLATES ARE LOCATED ABOVE THE QCM.

FIG. 4
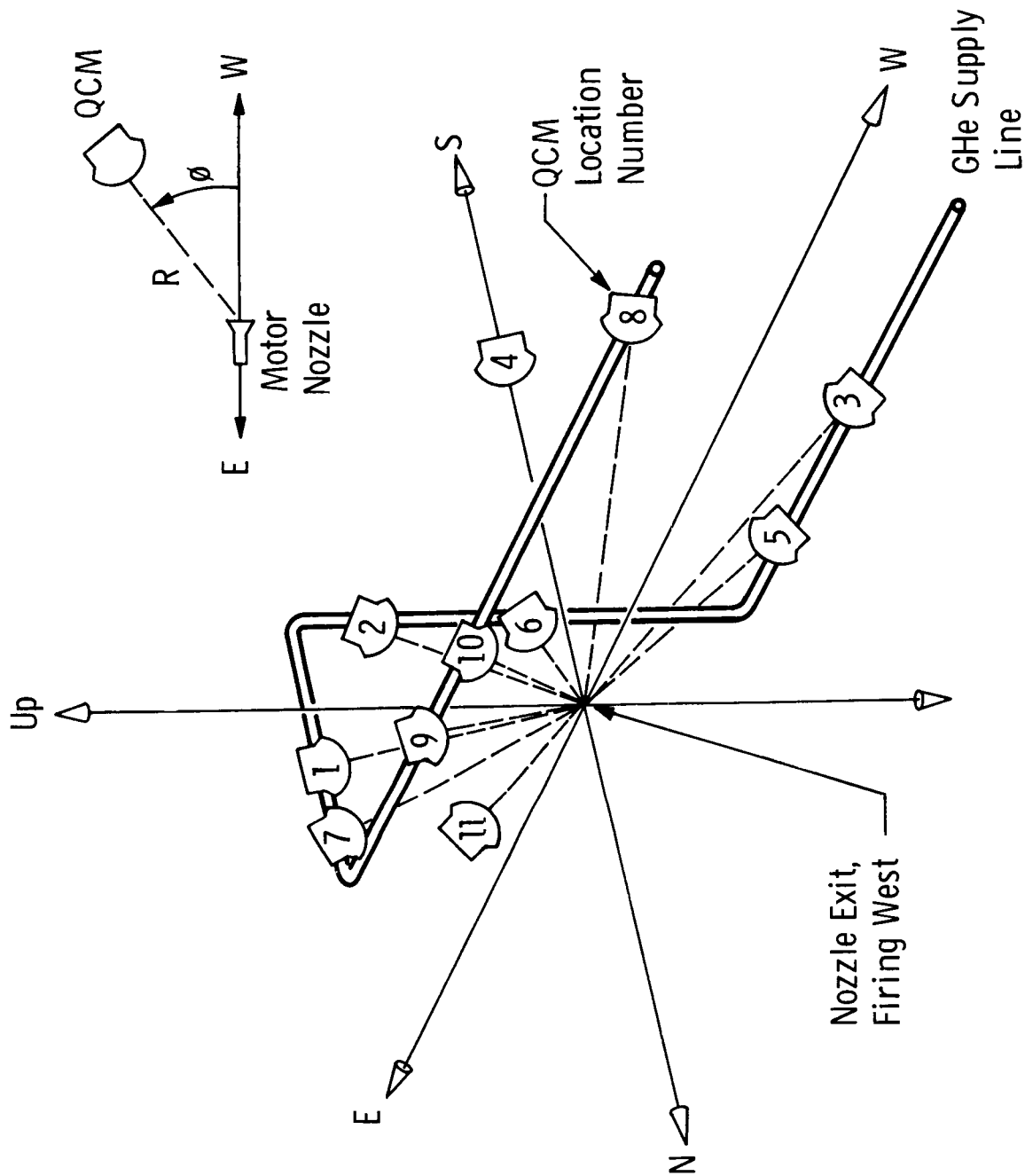
TYPICAL QCM LOCATIONS IN 10V CHAMBER

FIG. 5

d.   electron beam fluorescence for flowfield visualization.
The electron beam source is covered but visible in the extreme lower
left corner of Fig. 3.

e.   photography to detect sizeable droplets in the plume or a
propellant film layer inside the nozzle.

f.   ATR crystals and witness plates to collect hard contaminants
for residue analysis. An ATR crystal is located directly beneath the
thruster in Fig. 2. A variety of four witness plate collectors are
shown adjacent to the QCM in Fig. 4.

g.   solar cells to monitor degradation resulting from their
exposure to the plume. Ten solar cells mounted in a circular pattern
are located at the right edge of Fig. 3.

The primary emphasis of Phase II will be objective 3, characterizing
the thruster by measuring species concentration and temperature profiles
at the nozzle exit plane. Planned diagnostics include electron beam
fluorescence with an intensified vidicon system for measuring concentra-
tion and temperature profiles, a mass spectrometer on the plume centerline
to identify exhaust species, laser scattering to verify the absence of
droplets in the plume as indicated by the photography in Phase I, and
additional QCM measurements. Phase II will be completed this fiscal
year.

2.5 Test Summary - Phase I

The five engine configurations were fired over a wide range of
operating conditions as summarized in Tables 2, 3, and 4. Table 3 lists
baseline operating conditions and variations. Conditions were chosen
to reveal any effects these variables might have on the mass flux distri-
bution or hard contaminant levels in the plume. Varied parameters included
oxidizer to fuel ratio (O/F), duty cycle (δ), combustion chamber

TABLE 3

OPERATING CONDITIONS

Variable Parameter	Variations with Baseline Conditions Underlined
Oxidizer/Fuel (O/F)	1. 4, <u>1. 6</u>, 1. 8
Duty Cycle (δ), %	<u>1</u>, 2, 5, 10, Continuous
Comb. Chamber Pressure (P_c), psia	75, <u>100</u>, 125
Pulse Length (t_p), msec	25, 50, <u>100</u>, 200, 1000
QCM Temperature (T_x), $^\circ$K	<u>25</u>, 40, 75, 140, $\geq$180

TABLE 4

ENGINE FIRING SUMMARY

Firing Date	Config. Code	Engine Parameter Variations				QCM Temp. Variations	Total Pulses	Cumulative Firing Time (sec)
		O/F Ratio	δ (%)	P_c (psia)	t_p (msec)	T_x (°K)		
Oct 5	C	1.6	1	128	100	25 only	206	29
Oct 17-19	A	All	1, 10	All	All	25, 100, 160	3577	242
Nov 8-11	BL	All	All	All	All	All	4350	362
Nov 21-23	B	All	All	All	All	All	5024	387
Dec 6	D	1.6	2	100	100	All	1813	186

pressure (P_c), and pulse length (t_p). As indicated in Table 4, configurations A, BL (baseline), and B were tested most thoroughly.

Table 5 summarizes the measurements performed on each engine configuration. The QCM data is complete for all configurations, but somewhat limited on C and A. Coverage by the in situ IR transmission and laser interference measurements[19] was also thorough. Extensive IR transmission measurements were not attempted on configurations C and A because of intense interest in chamber and engine checkout at that point in time. Photography was done with a motorized 35 mm camera triggered by the firing sequencer through a microprocessor. Exposures were programmed to capture various portions of the firing pulse. The electron beam fluorescence species density measurement was limited to a proof-of-principle attempt in anticipation of extensive application in Phase II; it was successful. As discussed earlier the mass spectrometer was used in Phase I primarily for assessing chamber performance. It was not fast enough to obtain a complete scan over the mass number range of interest during a single pulse firing. Nevertheless some interesting partial scans were obtained, and extensive use of a mass spectrometer tailored for the plume measurement is planned in Phase II. Again the reader is referred to the project technical report, to be published, for complete results of all the measurements.

3.0 QUARTZ CRYSTAL MICROBALANCES

In the planning stage of this program, the intent was to use the QCM design which had performed successfully in the Jet Propulsion Laboratory (JPL) Molsink chamber for the monopropellant thruster contamination study[9, 10, 18]. After the JPL designs were reviewed, it was evident that

TABLE 5
SUMMARY OF MEASUREMENTS (PHASE I)

Measurement	Engine Configuration				
	C	A	BL	B	D
QCMs at Crystal Temperature (°K) 25	X	X	X	X	X
40			X	X	X
75			X	X	X
100		X	X	X	
140			X	X	X
180			X	X	
≥ 200			X	X	
Condensed Phase In Situ — IR Transmission for					
• Identification of Species Collected by QCMs at Same Temperature			X	X	X
• Optical Constants (n, k)			X		
— Laser Interference for					
• Cryodeposit Thickness	X	X	X	X	X
• Cryodeposit Density	X	X	X	X	X
• Index of Refraction at 0.6328 μm	X	X	X	X	X
IR Spectra of Gas Phase During Chamber Warm-Up			X	X	
E-Beam Fluorescence					
• Flow Visualization		X			
• Species Density (demo)					X
Photography			X	X	
ATR Spectroscopy	X	X	X	X	X
Witness Plates	X	X	X	X	X
Solar Cell Degradation		X	X	X	X
Mass Spectroscopy			X	X	

extensive modifications would be necessary to adapt the "low temperature" units which had been used to measure "far field" contamination. To meet the requirements of this study additional QCMs of the "variable temperature" design used by JPL to measure the mass flux within 30 deg of plume centerline were needed.
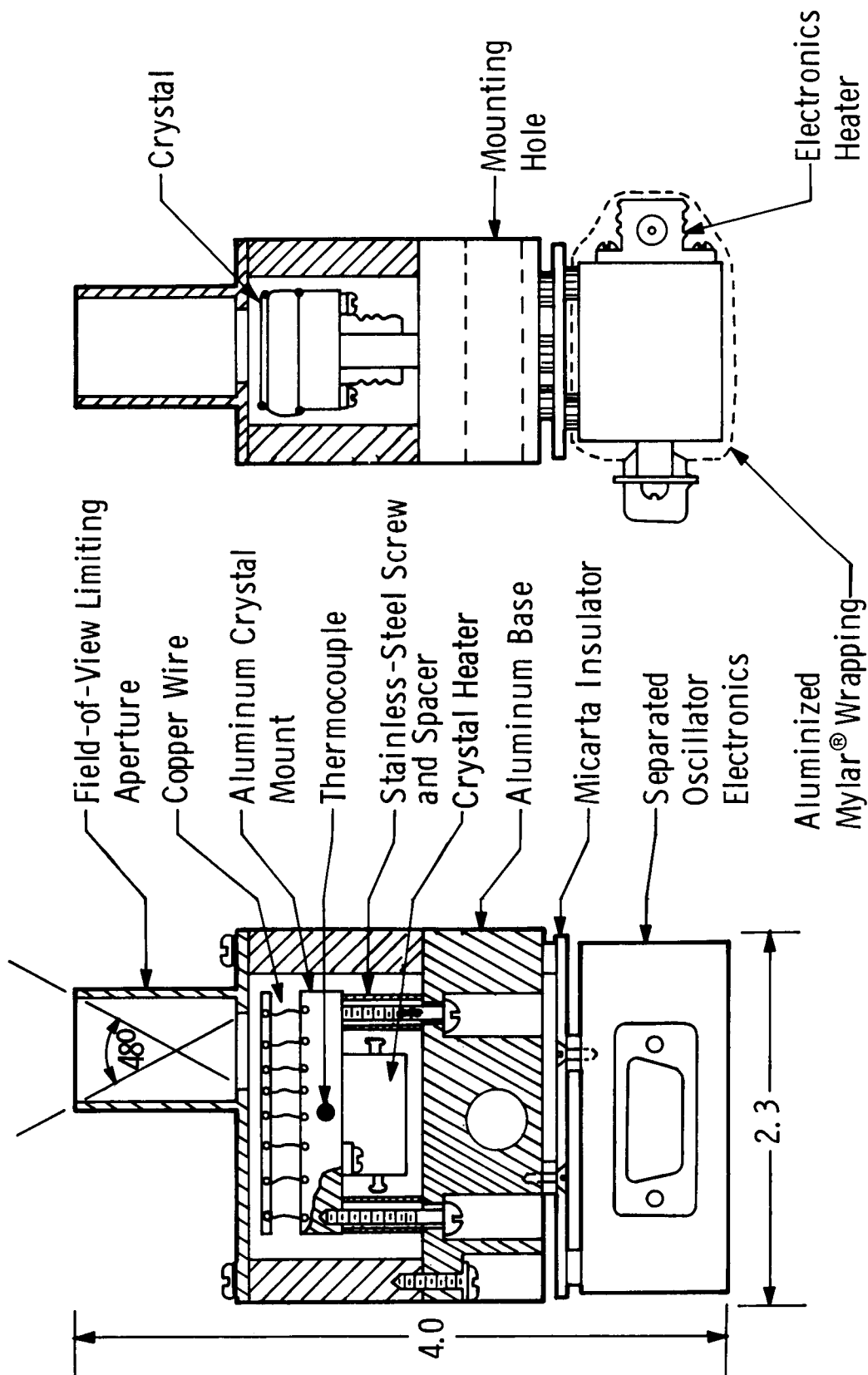
3.1 QCM Design

To determine the necessary design changes, one of the JPL variable temperature QCMs was operated in a small cryogenic vacuum chamber. In the present AEDC version (Fig. 6) the electronics package was insulated from the mounting and independently temperature controlled at near room temperature. The crystal was mounted on a temperature controlled heat sink connected to the QCM mounting block by a thermal conductor sized to allow a $20^{\circ}K$ to $300^{\circ}K$ temperature cycling in one hour with a heater power of 10W. With these two modifications, the QCM could be clamped to a constant low temperature heat sink, the crystal temperature controlled anywhere between the heat sink temperature and $300^{\circ}K$, and the oscillator electronics maintained at room temperature.

Crystals from some original JPL units were used, and additional crystals were purchased from the same vendor. Three of the crystals were cut at $39^{\circ}49'$ for a low temperature coefficient in the $77^{\circ}K$ range while the remaining nine were cut at $40^{\circ}28'$ for the range less than $40^{\circ}K$.

The oscillator and mixer circuit was modified only by adding an output stage with a gain of ten to improve the S/N when the QCMs are operated on long cables.

A field-of-view (fov) limiting aperture (see Figs. 4 and 6) was added to the cover plate on all QCMs, except one, to reduce the field-of-view to approximately $\frac{2\pi}{12}$ ster (48° full angle), and thereby to reduce

Crystal

Mounting Hole

Electronics Heater

Field-of-View Limiting Aperture

Copper Wire

Aluminum Crystal Mount

Thermocouple

Stainless-Steel Screw and Spacer

Crystal Heater

Aluminum Base

Micarta Insulator

Separated Oscillator Electronics

Aluminized Mylar® Wrapping

48º

2.3

4.0

QUARTZ CRYSTAL MICROBALANCE

FIG. 6

the molecular flux reaching the crystal from directions other than the nozzle. The QCM without a fov limiting tube was located at 90° from plume centerline adjacent to the cooled germanium substrate and used in conjunction with the IR transmission measurements.

Crystal temperature was taken to be that measured by a thermocouple imbedded in the heat sink to which the crystal was mounted (Fig. 6). The temperature of the QCM surroundings was less than $80^{\circ}K$, excluding the thruster nozzle directly in the field-of-view, and as a result of radiation exchange between the QCM and its surroundings, the crystal temperature was calculated to be within $0.1^{\circ}K$ of the heat sink temperature in the worst case.

3.2 QCM Operation

Eleven QCMs were installed in the chamber by clamping them to a stainless steel cryogenic line at various locations (see Figs. 3, 4, and 5 and Table 6) to achieve the desired angles between the plume centerline and the QCMs. With two exceptions, the QCMs were always pointed at the nozzle; QCM No. 1 ($\phi = 118^{\circ}$) was pointed downstream parallel to the plume centerline, and QCM No. 9 ($\phi = 62^{\circ}$) was pointed downstream toward the center of the LN_2 shield (Fig. 1). Neither of these QCMs had a geometrical view of the nozzle, the purpose being to measure backscattered flux during firing from directions other than the nozzle or antechamber door and to determine if significant back scattering from the plume and the cryopanels occurred.

The cryogen line to which the QCMs were clamped was cooled with nominal $20^{\circ}K$ GHe, allowing the QCM crystal temperatures to be controlled from $25^{\circ}K$ to $300^{\circ}K$. Several operating temperatures above $25^{\circ}K$ were chosen in order to selectively collect particular plume species (refer

TABLE 6
QCM LOCATIONS

Location No.	Oct 5, 1977 Configuration - C			Oct 17-19, 1977 Configuration - A			Nov 8-11, 1977 Configuration - BL			Nov 21 - Dec 6, 1977 Configuration - B, D		
	QCM No.	R (cm)	ø (deg)	QCM No.	R (cm)	ø (deg)	QCM No.	R (cm)	ø (deg)	QCM No.	R (cm)	ø (deg)
1	1	157	30	1*	76.7	109	1*	81.3	118	1*	79.0	115
2	2	112	45	2	61.7	117	2	66.8	131	2	63.6	128
3	3	91	60	3	91.4	60	3	81.0	69	3	83.0	66
4	4**	81	90	4**	82.3	81	4**	83.8	90	4**	80.7	87
5	5	79	90	5	78.7	90	5	72.6	101	5	71.8	97
6	6	56	118	6	50.8	111	6	55.9	127	6	53.0	123
7	12	81	108	12	81.3	108	12	76.2	117	12	74.0	114
8	8	91	90	8	91.4	90	10	155.0	26	10	159.6	25
9	9	104	60	9	104.1	60	9*	92.9	62	9	94.0	62
10	10	127	45	10	127.0	45	7	112.0	49	7	115.4	47
11	11	172	32	11	73.7	104	11	39.4	147	11	35.3	143
	7	Spare		7	Spare		8	Spare		8	Spare	

* QCMs Nos. 1 and 9 were pointed downstream toward the far end of the chamber away from the motor with no direct line of sight to the nozzle.

** QCM No. 4 was located as close as possible to the germanium substrate for the IR transmittance measurement. It did not have a collimating tube to limit the fov like the other QCMs.

to Tables 7 and 8). Data were recorded at the highest temperature first to avoid evaporation of previously condensed species, and thereby to shorten the measurement sequence.

When all of the QCM crystals had stabilized at the desired temperature, a set of QCM frequencies and temperatures was recorded; this was usually about ten minutes prior to the beginning of a sequence of engine firings. A second set was recorded just prior to the engine firing and a third set just after the firing sequence. If the data sets are designated 1, 2, and 3, respectively, the measured mass flux I is

$$I = \frac{d\dot{m}}{d\Omega} = \frac{KR^2 \Delta f}{N \, t_p}, \text{ gm/sec-ster} \tag{1}$$

where $\dot{m}$ = mass flux collected by QCM, gm/sec

Ω = solid angle subtended by the QCM fov, ster

K = QCM calibration constant[9] = 1.77×10^{-8} gm/cm^2 - Hz

R = distance from nozzle exit to QCM crystal, cm

$$\Delta f = (f_3 - f_2) - (f_2 - f_1)\frac{t_3 - t_2}{t_2 - t_1}, \text{ Hz} \tag{2}$$

N = number of engine firing pulses

t_p = pulse length, sec

t_i = time at which data were recorded, sec

During the firing sequence, QCM frequencies were monitored with a frequency-to-voltage converter and a strip chart recorder. Those QCMs which could accumulate sufficient mass during the sequence to saturate the crystal and stop oscillation were sampled first on the recorder so their data would not be lost. Data consisted of thermocouple voltages,

TABLE 7

CONDENSED MASS FRACTIONS*

QCM - R(cm) / -ø (deg) — T_X (°K)	155 / 26	112 / 49	81 / 69	73 / 101	56 / 127	67 / 131	Avg. Mass Fraction
≥180	0.025	0.021	0.021	0.010	0.017	0.012	0.017
140 - 180	0.383	0.412	0.380	0.398	0.371	0.266	0.368
75 - 140	0.138	0.123	0.175	0.122	0.196	0.345	0.183
40 - 75	0.111	0.117	0.150	0.185	0.211	0.109	0.147
25 - 40	0.343	0.327	0.274	0.285	0.205	0.268	0.285

*For the baseline engine configuration at baseline operating conditions (except averaged for t_p = 25 and 100 msec). These tabulated values were obtained by subtracting and normalizing the data plotted in Figs. 12a and 12b.

TABLE 8
BIPROPELLANT EXHAUST CONSTITUENTS COLLECTED AT VARIOUS TEMPERATURES

QCM Temp. (°K)	Cryopumped Species		Equilibrium Vapor Pressure* (torr) at QCM Temperature	Mass Fraction Measured at QCM Temperature	Mass Fraction Predicted for Major Species
180	Nitrate			0.017	
140	Plus	H_2O	4×10^{-9}	0.360	0.222
75	Plus	CO_2	8×10^{-9}	0.179	0.320
		N_2O	8×10^{-8}	} 0.54	} 0.54
		N_2O_4			
		NO_2			
		N_2O_3			
40	Plus	NO	4×10^{-12}	0.144	
25	Plus	N_2	8×10^{-8}	0.279 } 0.42	0.420
		CO	9×10^{-10}		0.004 } 0.44
		CH_4	8×10^{-13}		0.013
Not Collected	H_2			0.021 (Calculated)	0.021

*Compare to Chamber Pressure – 2×10^{-6} to 3×10^{-5} torr; Ref. 22

QCM output frequencies, sample number, sample time, and engine firing particulars such as pulse length, duty cycle, number of pulses in the sequence, combustion chamber pressure, and O/F ratio. When one or more QCMs stopped oscillating due to mass saturation, normally at frequencies between 50 and 100 kHz, the crystals were heated to 300^OK, and the frequencies were monitored until no further monotonic frequency change was evident. This process of cleaning the QCM crystals required a maximum of one hour.

4.0 RESULTS OF QCM MASS FLUX MEASUREMENTS

In this section results are presented in the form of plots comparing the measured mass flux per unit solid angle I (gm/sec-ster) for the various engine configurations and operating conditions. The oxidizer to fuel ratio (O/F), pulse duty cycle (δ), combustion chamber pressure (P_c), firing pulse length (t_p), and QCM crystal temperature (T_x) are specified in each case. Since comparisons by inspection only are often difficult, least squares exponential curves have been computed to fit appropriate sets of data. The slopes and intercepts (in semilog representation) for these exponential curves are always listed for the varied parameter, but the fitted lines are not always shown in order to avoid confusion on already busy figures. Instead a so-called "reference line" is shown on most figures; this is simply the least squares exponential fit to the data for all engine configurations at baseline operating conditions and $T_x = 25^O$K. As indicated in Fig. 7 the equation for the reference line is

$$I = 9.49 \; e^{-0.0752\phi} \; (\text{deg}) \tag{3}$$

It serves as a point of reference on each figure and accentuates the effect of any departure from the baseline operating conditions. At the same time the slope/intercept values can be used to detect any systematic changes in the measured mass flux resulting from the varied parameters.

Also on most figures a few backscatter measurements are plotted. These measurements indicate mass flux levels collected from viewing directions other than the nozzle during engine firing. This flux is attributed to molecular backscattering from either the cryogenic panels or the plume itself. The QCMs making these backscatter measurements were pointed downstream toward the far end of the chamber and had no direct line of sight to the nozzle. For ease of comparison with the other QCM measurements, these backscatter data have been plotted as if the QCMs were directed at the nozzle and located at the same R, ϕ coordinates (Table 6); i.e., the data is displayed as mass flux per unit solid angle rather than mass flux per unit area.

This is also an appropriate time to point out that the QCM locations were staggered with about half mounted on each side of the chamber or nozzle centerline, yet the measured flux values show no evidence of asymmetry in the plume. Therefore the nozzle geometrical axis and the plume centerline are taken to be identical, and all QCM data is plotted at positive angles.

4.1 Effect of Varying Engine Configurations

Data was obtained on all five engine configurations operating at baseline conditions (see Tables 3 and 4), and the results are plotted in Fig. 7. Under these firing conditions the five configurations produced remarkably similar mass flux levels and angular distributions. These combined data for the five configurations, like all the QCM mass
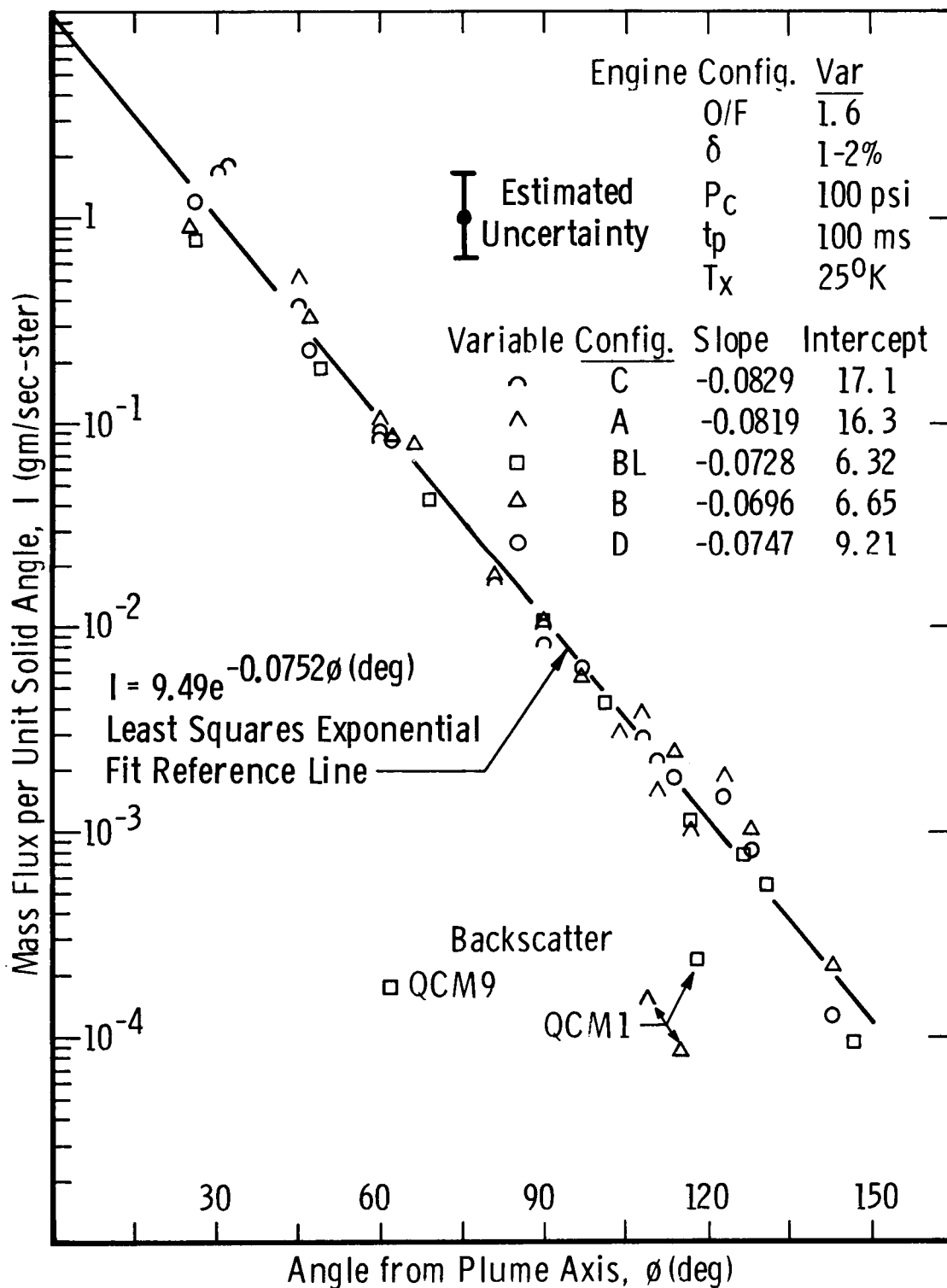
Fig. 7 Mass Flux for Various Engine Configurations at Baseline Operating Conditions

flux measurements obtained in this program, exhibit an exponential
dependence on ϕ, the angle from the plume centerline. Nearly all
measured values fall within a factor of two of the exponential line
fitted to the combined data points, and thereby justify the use of
exponential curve fitting. In addition to the curve fitted to the
combined data, slopes and intercepts are listed in Fig. 7 for the
exponential curves fitted to the data for each engine configuration.
Although the slopes and intercepts are all very close, the manner
in which C and A agree but differ from the remaining configurations
is eye-catching because it correlates with the chronological sequence of
relocating the QCMs (Table 6). In spite of this observation, the
general conclusion drawn from Fig. 7 is that these measurements
reveal no significant differences in the mass flux distributions
for the five engine configurations tested.

4.2 Effect of Varying Engine Operating Conditions

Figs. 8, 9, and 10 show the results of varying the oxidizer to
fuel ratio - 1.4 to 1.8, the duty cycle - 1 to 10%, and the combustion
chamber pressure - 75 to 127 psia for the baseline engine configuration.
No pronounced effects on the measured mass flux are apparent, except
a hint in Fig. 10 that the flux at the low angles was slightly higher
for higher P_c.

Figs. 11a and 11b illustrate the effect of varying the firing pulse
length from 25 msec to 1 sec (there were also a few 2 sec firings) for
two engine configurations. Inspection of either the listed slopes/
intercepts or the plotted points reveals a consistent increase in the
measured mass flux as the pulse length decreased. The increase is less
than a factor of two but was quite reproducible for all engine configura-
tions. The constant slope tells us the effect does not depend on angle.
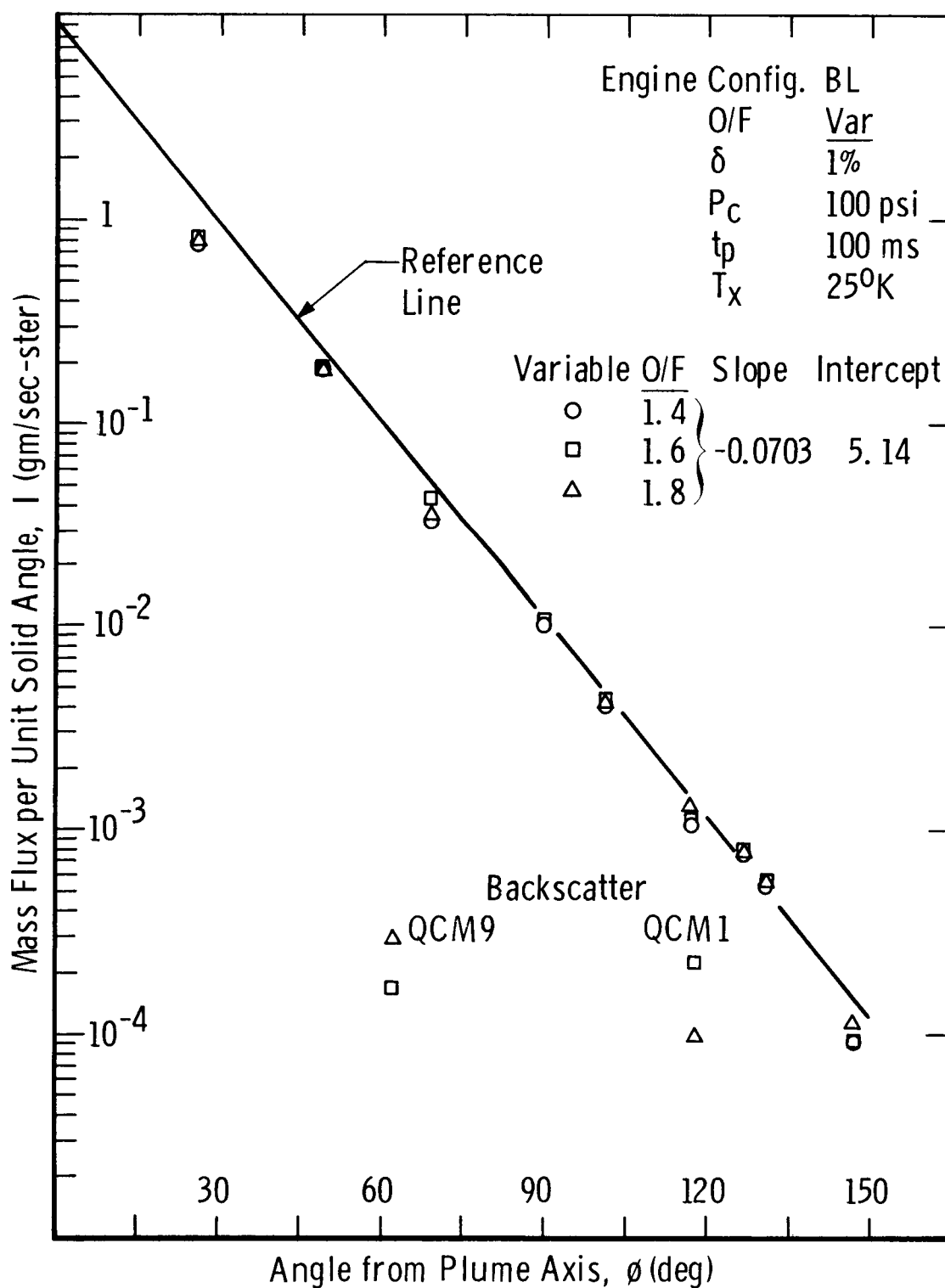
713

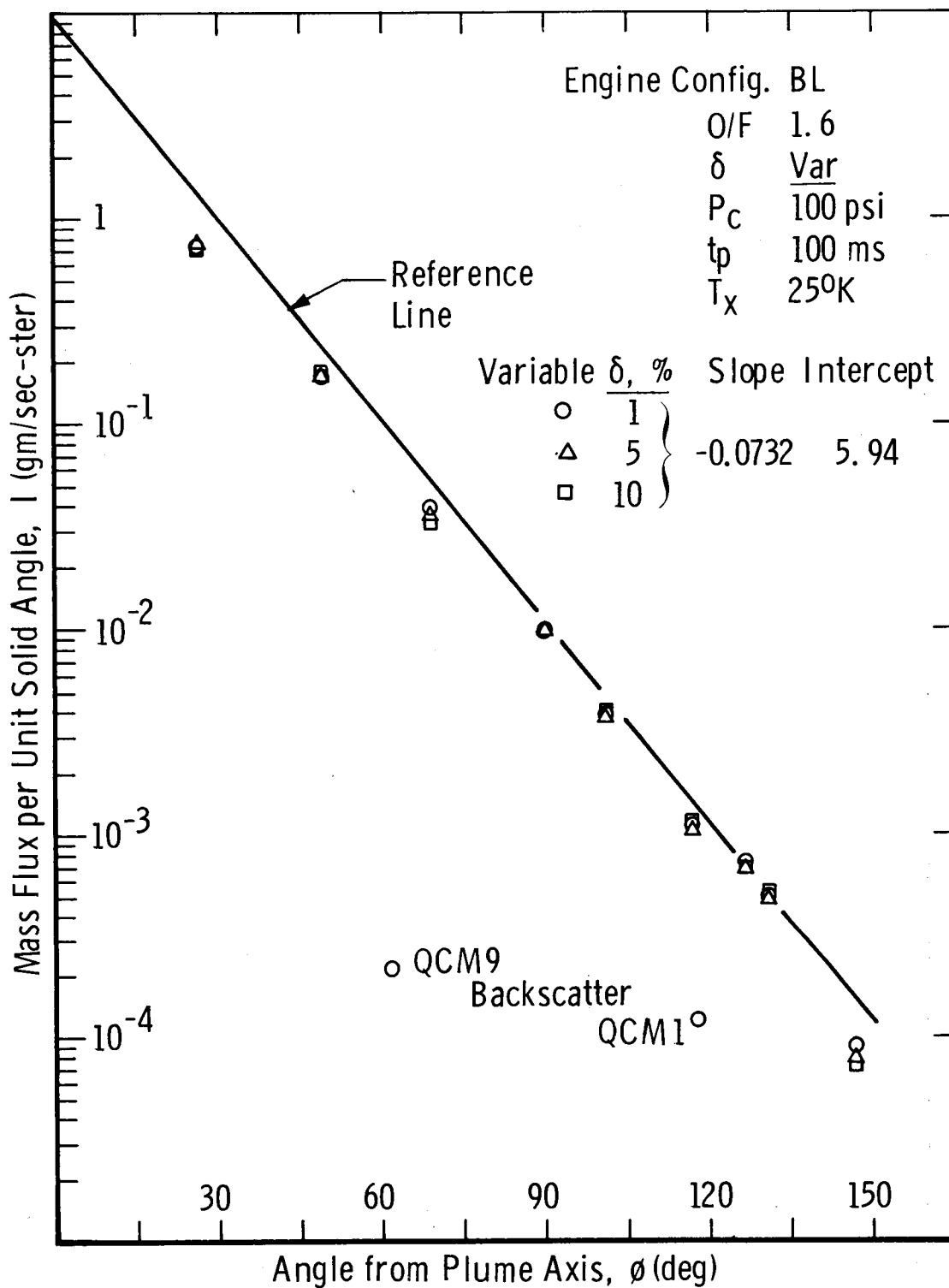Fig. 8 Effect of Oxidizer to Fuel Ratio; Baseline Engine

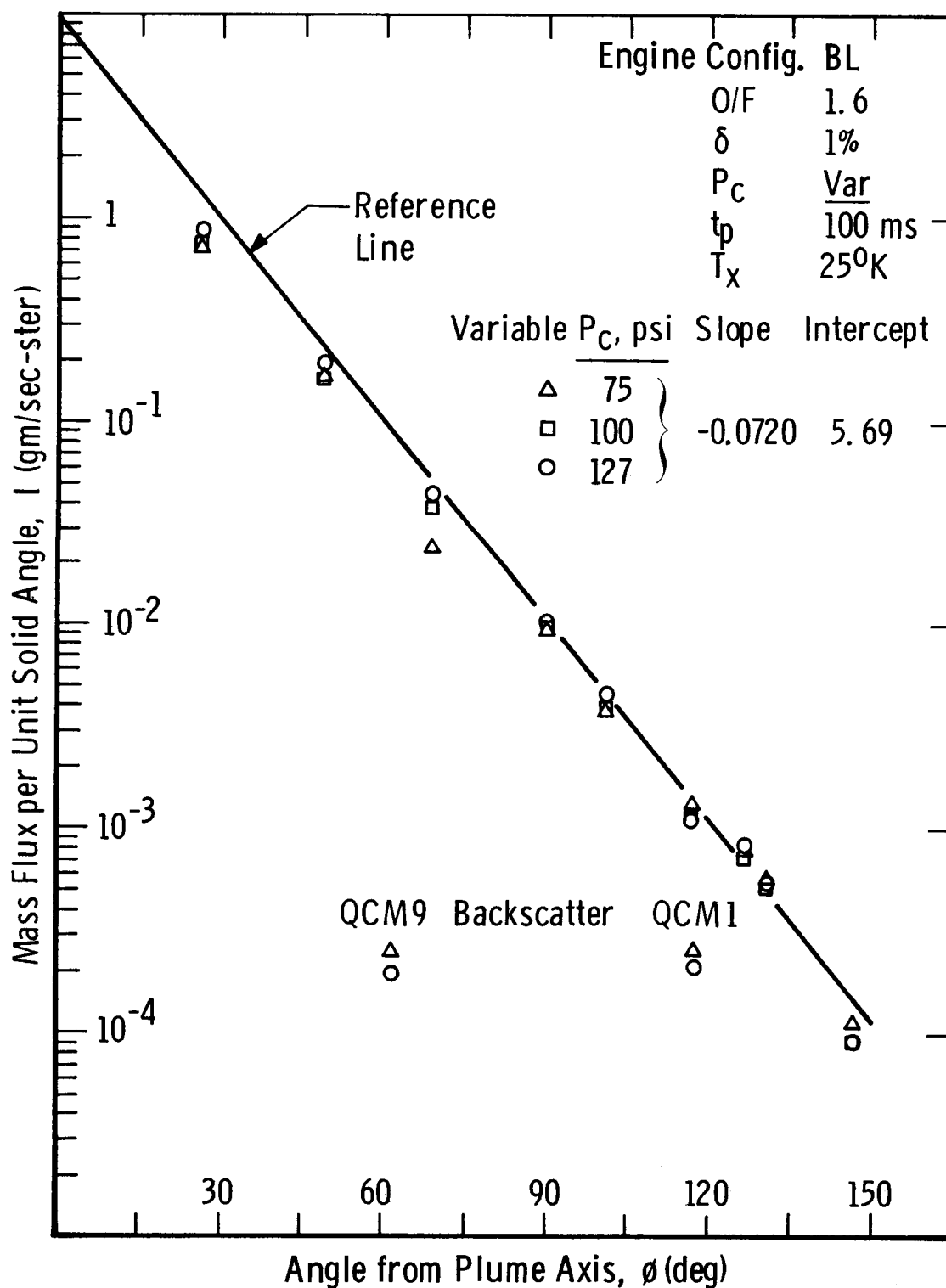Fig. 9 Effect of Duty Cycle; Baseline Engine

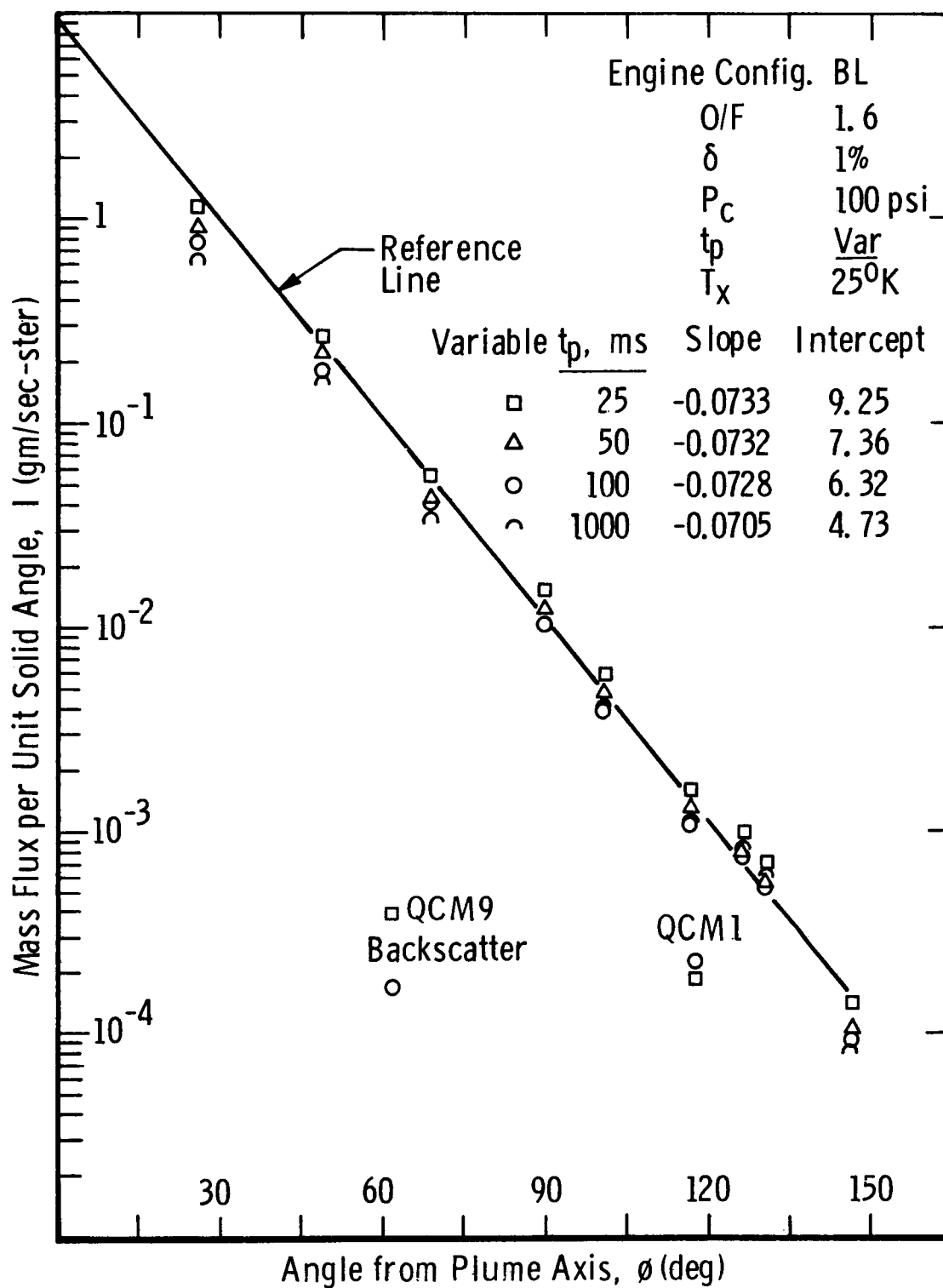Fig. 10 Effect of Combustion Chamber Pressure; Baseline Engine
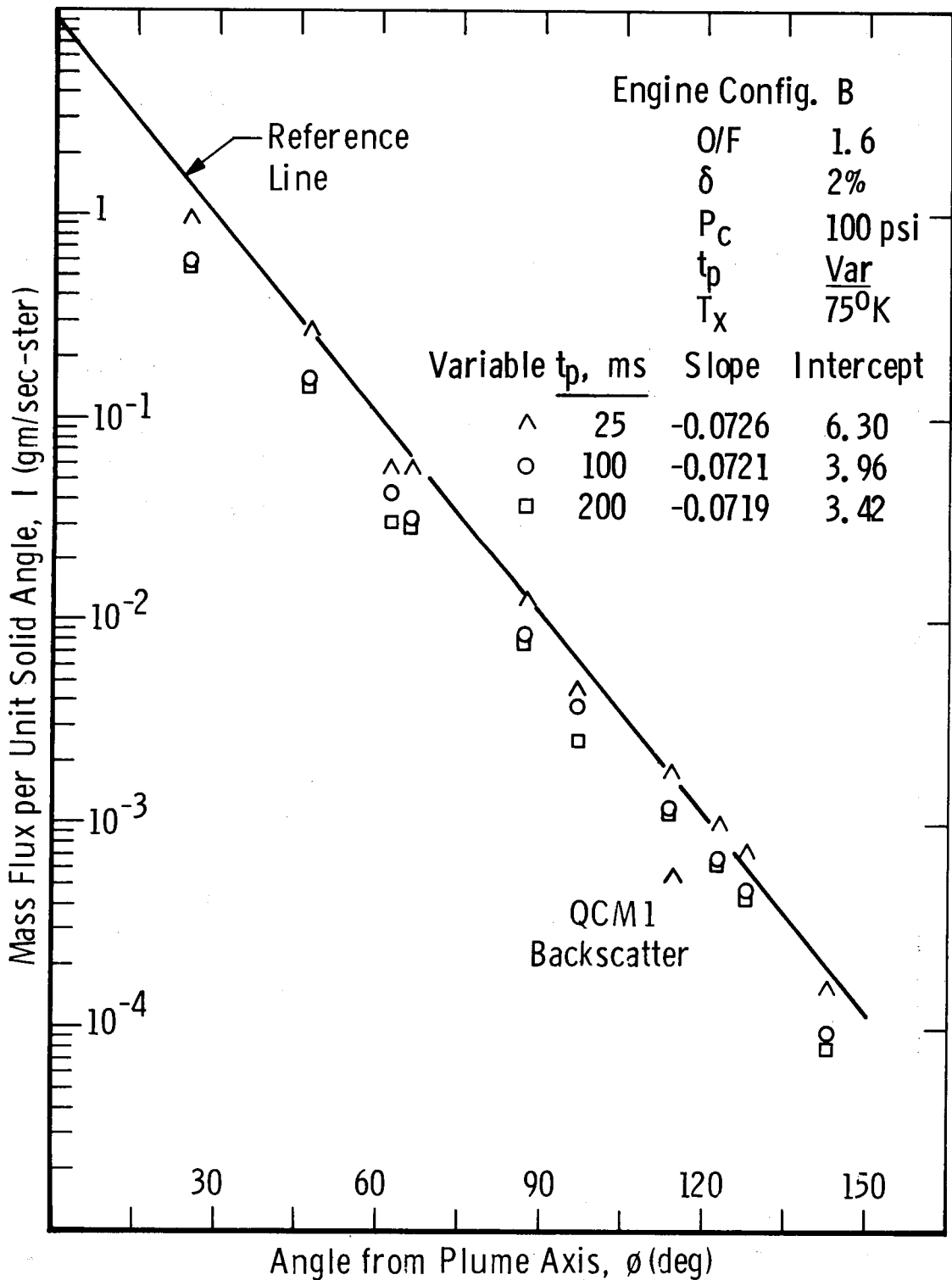
Fig. 11a Effect of Pulse Length; Baseline Engine

Fig. 11b Effect of Pulse Length; Engine Configuration B
and Crystal Temperature 75°K

Moreover, the change in intercept is expected if higher mass flux levels are associated with engine ignition and shut down, in which case the mass flux from the thruster depends on the number of pulses making up the accumulated firing time.

4.3 QCM Temperature Variation

Figs. 12a, 12b, and 12c compare the mass flux collected at the various QCM operating temperatures. In these figures the fitted exponential lines are shown explicitly. The fitted line intercepts decrease in a well-behaved and predictable manner as the crystal temperature (T_x) increases, simply indicating that fewer exhaust species were cryopumped at the higher temperatures. Notice the sharp drop (about two orders of magnitude) in collected mass flux when the crystal temperature increases from 140 to 200°K. The species collected at T_x > 180°K are more readily referred to as contaminants in the usual sense because no major bipropellant combustion products condense at such high temperatures. Fig. 12c confirms that the products collected at 200°K were coming from the thruster and were not temporarily trapped species which would evaporate in time. From present indications (IR spectra) these were nitrates and represent potential spacecraft contaminants. Witness plate samples will be used to verify this identification.

As mentioned earlier the in situ IR transmission measurement was carefully planned to help determine[†] the QCM operating temperatures and to identify the IR active species which were collected at each temperature. The identified exhaust species and the crystal temperatures chosen to selectively cryopump the major species are listed in Table 8; also the

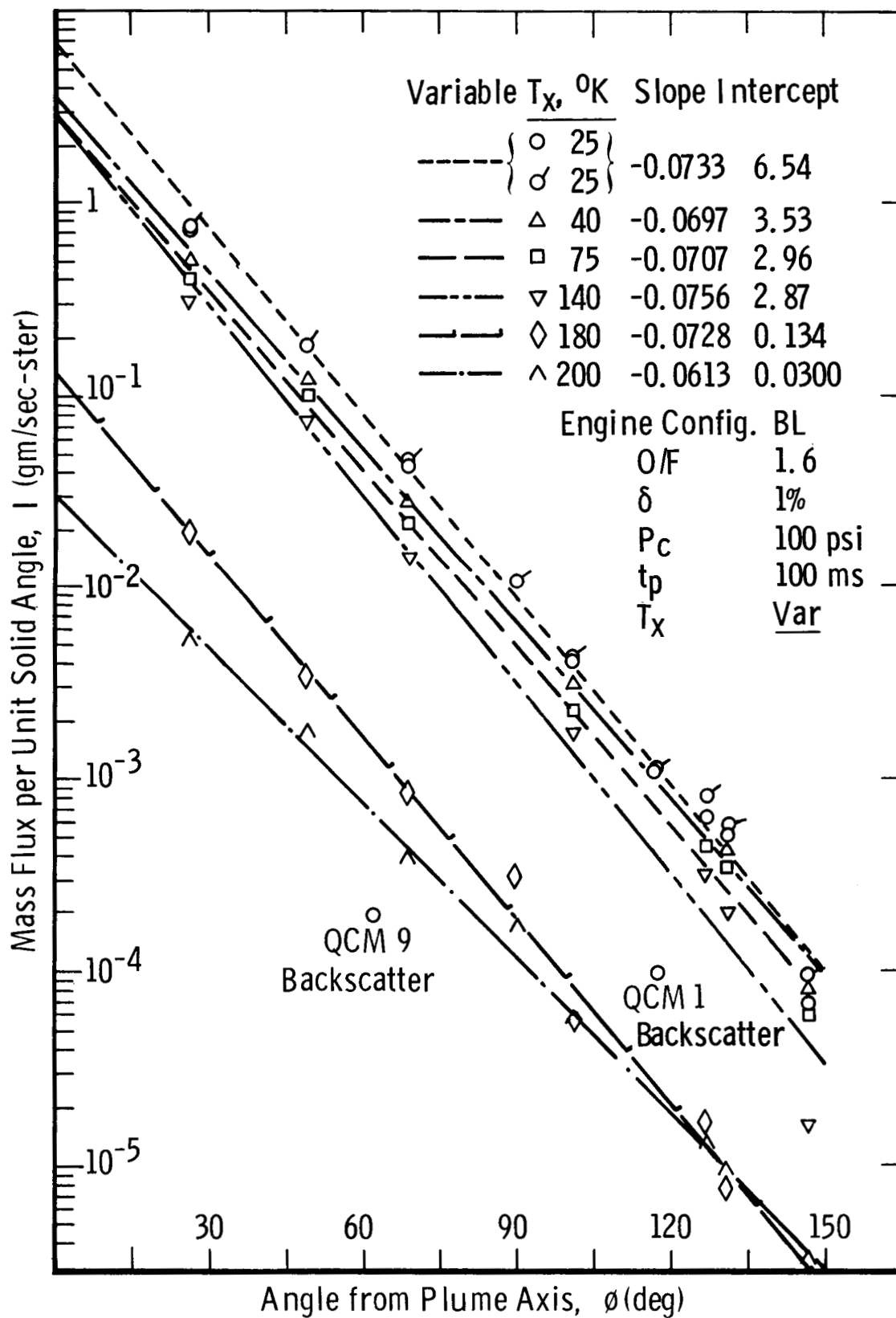[†]Along with equilibrium vapor curves which are frequently not available for plume species.

Fig. 12a QCM Temperature Variation; Baseline Engine
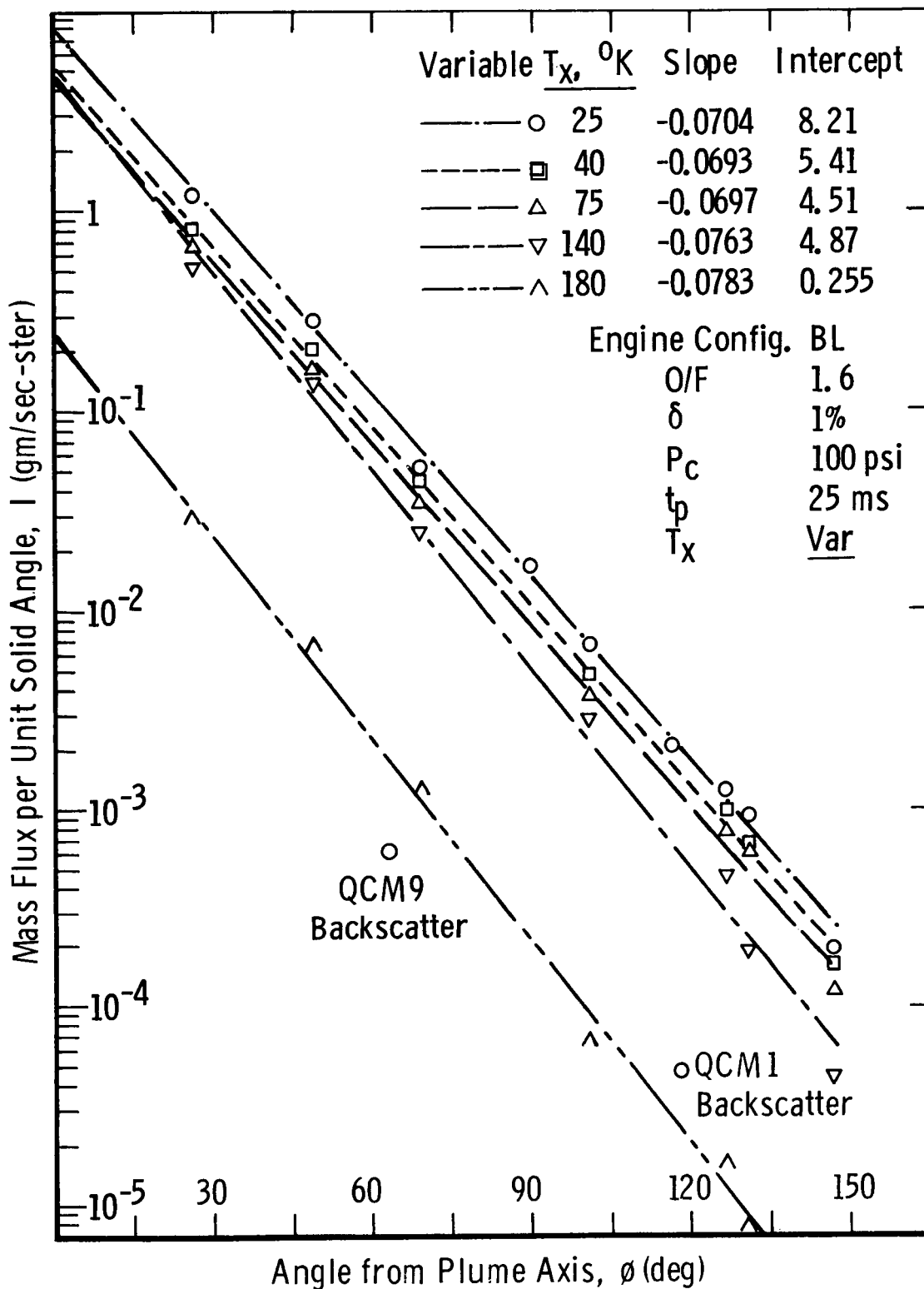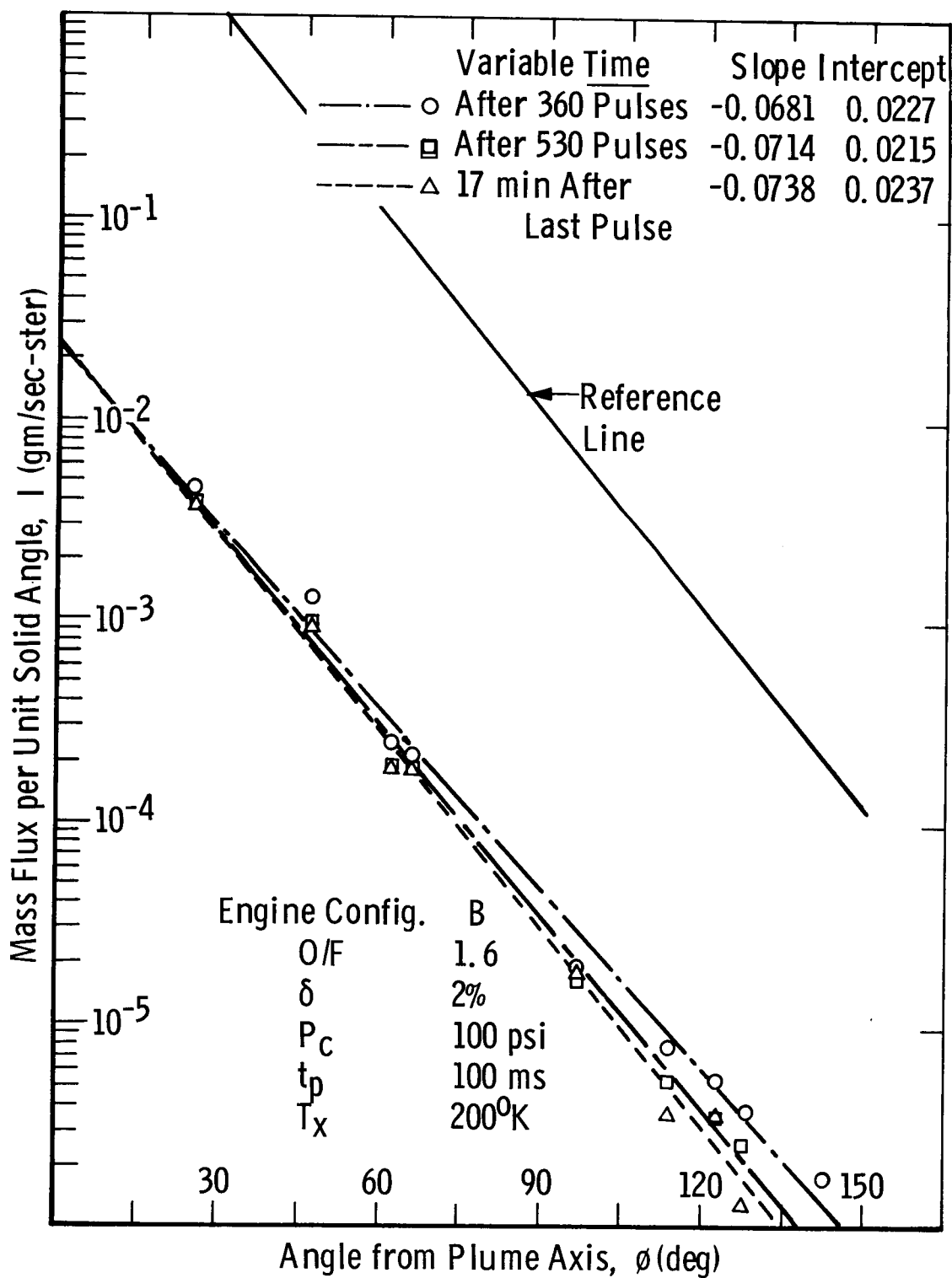
Fig. 12b QCM Temperature Variation; Pulse Length 25 msec

The figure plots Mass Flux per Unit Solid Angle, I (gm/sec-ster) versus Angle from Plume Axis, ø (deg).

Variable T_X, °K	Slope	Intercept
○ 25	-0.0704	8.21
▣ 40	-0.0693	5.41
△ 75	-0.0697	4.51
▽ 140	-0.0763	4.87
∧ 180	-0.0783	0.255

Engine Config.	BL
O/F	1.6
δ	1%
P_C	100 psi
t_p	25 ms
T_X	Var

QCM9 Backscatter

QCM1 Backscatter

721

Fig. 12c Evaporation at Crystal Temperature 200°K

available equilibrium vapor pressures[22] are given. When only major constituents are considered, Table 8 indicates that H_2O is collected at $140^{\circ}K$, $H_2O + CO_2$ at $75^{\circ}K$, and $H_2O + CO_2 + N_2$ at $25^{\circ}K$. Then by subtracting and properly normalizing the mass flux collected by each QCM at this series of operating temperatures, one obtains the approximate mass fractions of major species found in the bipropellant exhaust plume.

The above approach was used to generate the condensed mass fractions given in Table 7 from the same data plotted in Figs. 12a and 12b. Of course the values listed in Table 7 do not include H_2 which does not condense at $25^{\circ}K$. From an equilibrium computation for very similar engine operating conditions, we obtained a predicted mole fraction for H_2 of 0.231 which converts to a mass fraction of 0.021. Then the average values listed in Table 7 were renormalized, assuming this mass fraction of uncollected H_2, to get the measured mass fractions listed in Table 8. Also, in Table 8, the remaining mass fractions predicted by the equilibrium computation are shown for comparison. Although the measured and predicted values at each QCM temperature do not agree well, there is general agreement for the total fractions collected above and below $75^{\circ}K$, as indicated by the braces in Table 8. The same "washed-out" temperature dependence is also illustrated in Fig. 12d where relative condensed mass fraction versus crystal temperature is plotted. There are sharp jumps as expected in the condensed mass at the temperatures where H_2O and N_2 condense, but there are no similar steps in the data between $60^{\circ}K$ and $140^{\circ}K$, conspicuously not at $86^{\circ}K$ where CO_2 should condense. In fact Fig. 12d shows that CO_2 and H_2O are not well separated. Most likely this observed smoothing is due to CO_2 cryosorption by H_2O cryodeposits.
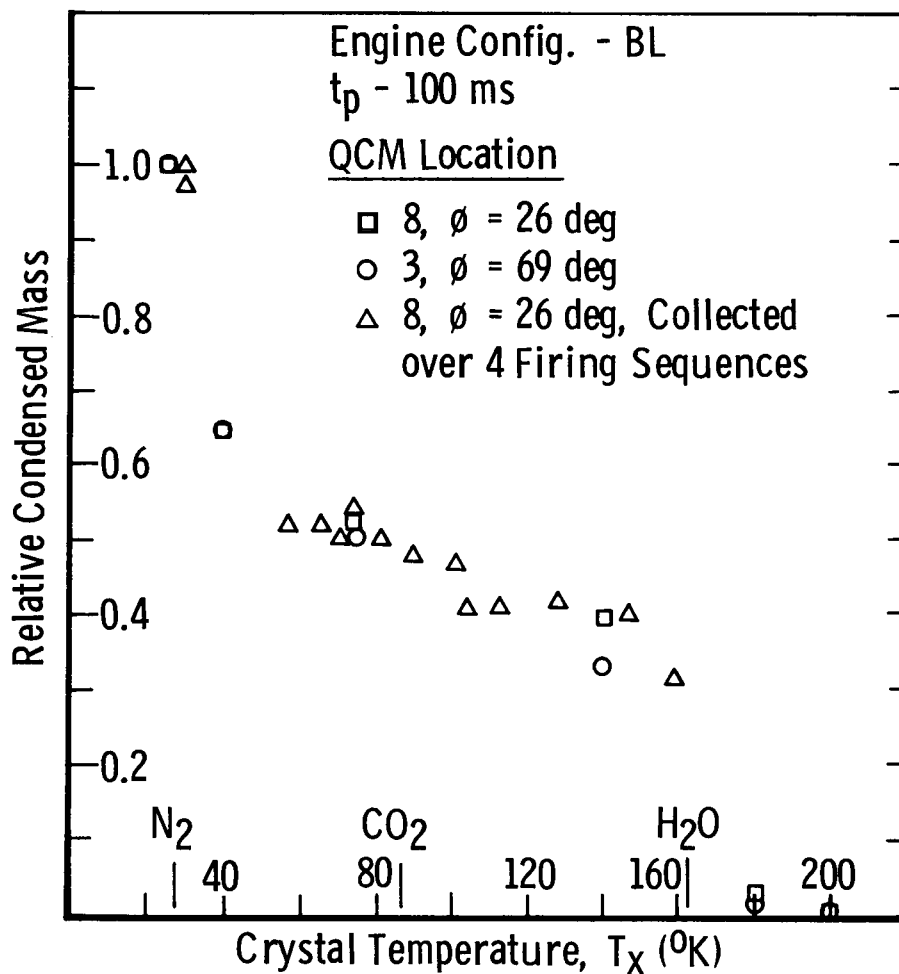
723

Fig. 12d Relative Mass Collected as Function of
Crystal Temperature

One final observation is based on Figs. 12a and 12b. The slopes of the fitted lines for the mass flux collected at the intermediate crystal temperatures, $40^\circ K$ and $75^\circ K$, are consistently lower than those for $25^\circ K$ and $140^\circ K$. This suggests that the CO_2 and other species collected at the intermediate temperatures are relatively more abundant at higher angles than the N_2 and H_2O collected at $25^\circ K$ and $140^\circ K$ respectively. The point is more apparent in Table 7 where the condensed mass fractions for the $75 - 140^\circ K$ range tail up at the higher angles. This effect could be explained by a higher concentration of CO_2 in the boundary layer. Hopefully an explanation, or at least some clarification, will be provided by nozzle exit plane concentration profiles obtained in Phase II.

4.4 Assessment of Results

4.4.1 Chamber Performance

As stated before, the importance of a sufficiently long mean free path to the measurement of mass flux in the plume backflow region was recognized. A reduced mean free path resulting from an increase in vacuum chamber pressure during a firing sequence would invalidate the measurements. To determine the effect on the QCM data, the chamber pressure was systematically increased by adding helium. The QCM data obtained while performing this stepwise increase in chamber pressure is presented in Fig. 13 where the tabulated pressures (P_{He}) take into account the gauge factors for hydrogen and helium. The lowest pressure listed was the case before the addition of helium began, and the residual gas was assumed to be mostly hydrogen. There was no significant change in the QCM data after adding the first increment of helium. Further increases in chamber pressure up to 8.4×10^{-4} torr, a factor of 200 times the lowest pressure, caused only a factor of three decrease in
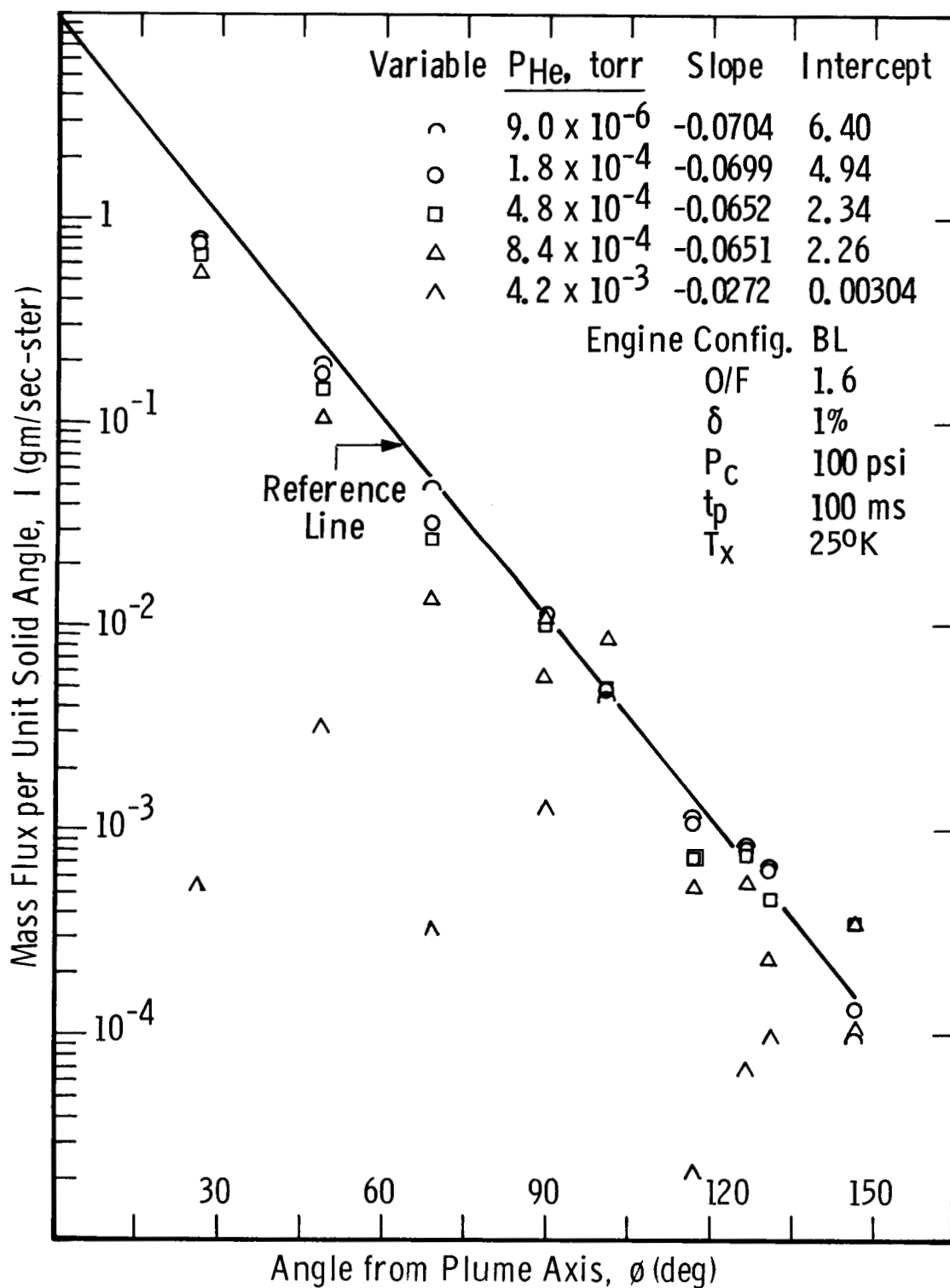
725

Fig. 13 Effect of Cryogenic Chamber Pressure

the collected mass flux. Finally, when the chamber pressure was increased to 4.2×10^{-3} torr, the results became very erratic. For comparison, the typical chamber pressure during a firing sequence was 3×10^{-5} torr. This experiment demonstrated that the cryogenic chamber performance was more than adequate and that the chamber had no measurable effect on the mass flux measurements.

4.4.2 Random and Systematic Error

One challenge associated with the mass flux measurements was to produce repeatable conditions for each engine configuration such that results might be meaningfully compared to one another and to theory. Such experimental realities introduced several sources of error into the mass flux measurements. These sources of error are discussed below.

Random error can be estimated from the data. Because there were insufficient data at identical test conditions to provide a meaningful statistical base, several sets of data which included variations in test conditions that did not strongly affect measured results were combined. Measurements on engine configuration A at six angles for five firing sequences were analyzed. Test conditions were $T_x = 25^\circ K$, $t_p = 100$ msec, $O/F = 1.6$, $\delta = 1$ to 5%, $P_c = 75$ to 125 psia. Relative standard deviation at each angle ranged from 5.9 to 10.4%. Similar data for engine configuration B was analyzed with relative standard deviations ranging from 4.8 to 15.1%. Thus, the random error in the QCM measurements is estimated at $\pm$ 10%.

Systemic error in the measured values of I can be estimated by differentiating the functional relationships between I and the measured parameters. These include Eq. (1) and the experimentally determined relation (Eq. (3). Quite generally for the purpose of error analysis

$$I = I(R, \phi, K, \Delta f, T_x, \Omega, N, t_p, O/F, \delta, P_c) \tag{4}$$

where all symbols have been defined earlier. Treating these measured parameters in order:

R - distance from nozzle exit plane to QCM location

$$\frac{1}{I} \frac{\partial I}{\partial R} \Delta R = -\frac{2 \Delta R}{R} = -\frac{2 \, cm}{40 \, cm} = -0.05 \qquad (5)$$

ϕ - angle from plume axis to QCM location

Using Eq. (3)

$$\frac{1}{I} \frac{\partial I}{\partial \phi} \Delta \phi = -0.0752 \, \Delta \phi = -0.15 \qquad (6)$$

K - QCM calibration constant

$$\frac{1}{I} \frac{\partial I}{\partial K} \Delta K = 0.5 \qquad (7)$$

This estimate of uncertainty in K is based on our effort to calibrate the set of QCMs at $25^{O}K$ in a molecular beam chamber with CO_2.

Δf - change in QCM frequency during engine firing sequence

Measured frequencies were probably within 1 Hz. However, jumps in crystal frequency as condensed mass accumulated could have caused errors. During initial checkout frequency jumps less than 200 Hz were observed in several QCMs. Large jumps of several kHz were also observed in a few QCMs, but in the data reduction these would have been recognized as bad points. Since most frequency changes measured during a firing sequence were less than 200 Hz, jumps usually appeared as questionable or obviously bad data; there were not a large number of these questionable data points.

At the higher angles and crystal temperatures the measured change in crystal frequency was only a few hertz. Resolution in the measurement of I was determined by a frequency resolution of 1 Hz

and the firing time. Therefore, the noise equivalent mass flux per unit solid angle (NEI) for a typical 10 sec firing sequence is estimated to be

$$NEI = \frac{K R^2 (\Delta f = 1)}{N t_p} = 2.75 \times 10^{-6} \text{ gm/sec-ster} \tag{8}$$

In practice, background mass flux prevented this NEI from being realized; the actual NEI was closer to 1×10^{-5} gm/sec-ster.

T_x - QCM crystal temperature

Condensed mass depends strongly on crystal temperature near those temperatures where major species have sufficiently high vapor pressure to evaporate (see Table 8). Since these temperatures were avoided, there should be little error associated with T_x. The one exception was the lowest temperature (25°K) which is close to the point at which N_2 evaporates. For an estimated fraction of N_2 not collected, we will use the difference between the predicted and measured mass fractions at 25°K from Table 8. Thus

$$\frac{1}{I} \frac{\partial I}{\partial T_x} \Delta T_x = -0.16 \tag{9}$$

Ω - QCM field-of-view

Measured values of I depended on the fov to some extent, more so at the higher angles where the absolute values approached the backscattered mass flux levels. During the firing of engine configurations B and D, QCM No. 9 at 62° had no fov limiting tube, yet the measured values shown in Fig. 11b were not perceptably greater. However, during the firing of engine configuration BL, when QCM No. 1 (118°) and No. 9 (62°) were pointed downstream with no line of sight to the nozzle, they measured 14% and 0.3% respectively (Fig. 8) of the flux they

would have measured if pointed directly at the nozzle. Apparently there was flux from directions other than the nozzle., and at large angles the flux outside the fov exceeded that within the fov, when viewing the nozzle, by a factor of two. Nevertheless, since the objective was to measure I with identical fields-of-view at all angles, the small differences in the fields-of-view of the various QCMs and the small errors in pointing direction had a negligible effect on I.

t_p - firing pulse length

At a programmed pulse length of 25 msec, the actual firing time determined from records of P_c was about twice as long. At longer programmed pulse lengths (> 100 msec), the actual firing time matches the programmed length more closely. The actual firing time is considered a characteristic of the engine, and the appropriate error is associated with the programmed pulse length. For t_p = 25 msec and Δt_p = 0.002 msec

$$\frac{1}{I} \frac{\partial I}{\partial t_p} \Delta t_p = - \frac{0.002 \text{ msec}}{50 \text{ msec}} = -4 \times 10^{-5} \tag{10}$$

P_c - combustion chamber pressure

From the measured values the change in I was less than 25% for a change in P_c from 75 to 125 psia. For ΔP_c = 5 psia,

$$\frac{1}{I} \frac{\partial I}{\partial P_c} \Delta P_c = \frac{0.25 \times 5 \text{ psia}}{50 \text{ psia}} = 0.025 \tag{11}$$

The estimated uncertainty in N is zero, and changes on O/F and duty cycle (δ) had no significant effect on I. Finally then, the total systematic error in the mass flux measurements is obtained by combining the errors of unknown sign randomly and errors of known sign algebraically.

$$\frac{\Delta I}{I} = 0.16 \pm \left[\overset{T_x}{(0.05)^2} + \overset{R}{(0.15)^2} + \overset{\phi}{(0.5)^2} + \overset{K}{(4 \times 10^{-5})^2} + \overset{P_c}{(0.025)^2} \right]^{\frac{1}{2}}$$

(12)

Note that most of the systematic error is the result of uncertainty in the QCM calibration constant. The assigned uncertainty in K is based solely on our partially completed effort to calibrate the QCMs at 25°K. It does not seem reasonable to expect so much uncertainty in K for these QCMs.

The random error is insignificant compared to the systematic error, so the total error estimate is

$$\frac{\Delta I}{I} = \begin{cases} \pm 0.53 & \text{for } T_x \geq 40^{\circ}K \\ 0.16 \pm 0.53 & \text{for } T_x = 25^{\circ} K \end{cases}$$

(13)

4.4.3 Comparison with Analytical Predictions

As pointed out in the introduction CONTAM does not incorporate a boundary layer model and, therefore, does not expand the flow field properly to predict mass flux in the backflow region. It would seem then the most worthwhile assessment for us to make here is to compare the experimental data to both an inviscid model and a boundary layer model. Such a comparison could be of value in providing direction to upcoming model improvement efforts. For the inviscid model prediction it is convenient to use the cosine law approximation[23, 24, 26] to the method of characteristics (MOC), and for the boundary layer model Simons[26] has developed simple closed-form expressions for Boynton's numerical treatment[25] of the supersonic portion of the nozzle boundary layer. It should be clearly understood at the outset that these are only first-order estimates for the purpose of comparison.

Boynton's work suggests that at large angles from the nozzle axis the plume gas density obeys an exponential decay law. Based on Boynton's results, Simons[26] assumed the cosine law is valid for angles less than some angle ϕ_o, and the exponential applies for angles greater than ϕ_o, where ϕ_o is the turning angle for the streamline at the edge of the boundary layer. Using this approach Simons obtained the following analytical forms for the gas density distribution:

$$f(\phi) = \cos^{2/(\gamma-1)} \left[(\pi/2)(\phi/\phi_\infty) \right] \text{ for } \phi < \phi_o \qquad (14)$$

where γ is the ratio of specific heats, and ϕ_∞ is the value of the limiting turning angle for an inviscid supersonic flow.

$$f(\phi) = f(\phi_o) \, e^{-\beta(\phi - \phi_o)} \text{ for } \phi > \phi_o \tag{15}$$

where ϕ_o and β are functions[26] of the nozzle exit conditions. ϕ_o is related to the boundary layer thickness (δ_e) through

$$f(\phi_o) = (2\delta_e/R_e)^{2/(\gamma + 1)} \tag{16}$$

where R_e is the nozzle exit radius.

For evaluating Simons' equations, the appropriate parameter values for the 5 lb_f thruster (baseline configuration) were determined to be:

Ratio of specific heats, $\gamma = 1.25$

Effective nozzle area ratio, $A_e/A_t = 84$

Exit Mach number, $M_e = 5.2$

Combustion chamber pressure, $P_c = 100$ psia

Combustion chamber temperature, $T_c = 2500^\circ K$

Then the numerical values of Simons' parameters are:

$$\phi_o = 22.06^\circ$$

$$\phi_\infty = 75.8^\circ$$

$$f(\phi_o) = 0.42$$

$$\beta = 8.93$$

$$\delta_e/R_e = 0.188$$

The resulting mass flux distributions predicted by the inviscid and boundary layer models are plotted in Fig. 14 with the experimental data, Eq. (3), for comparison. As expected the inviscid prediction falls off much too fast. Furthermore, the boundary layer prediction also decays
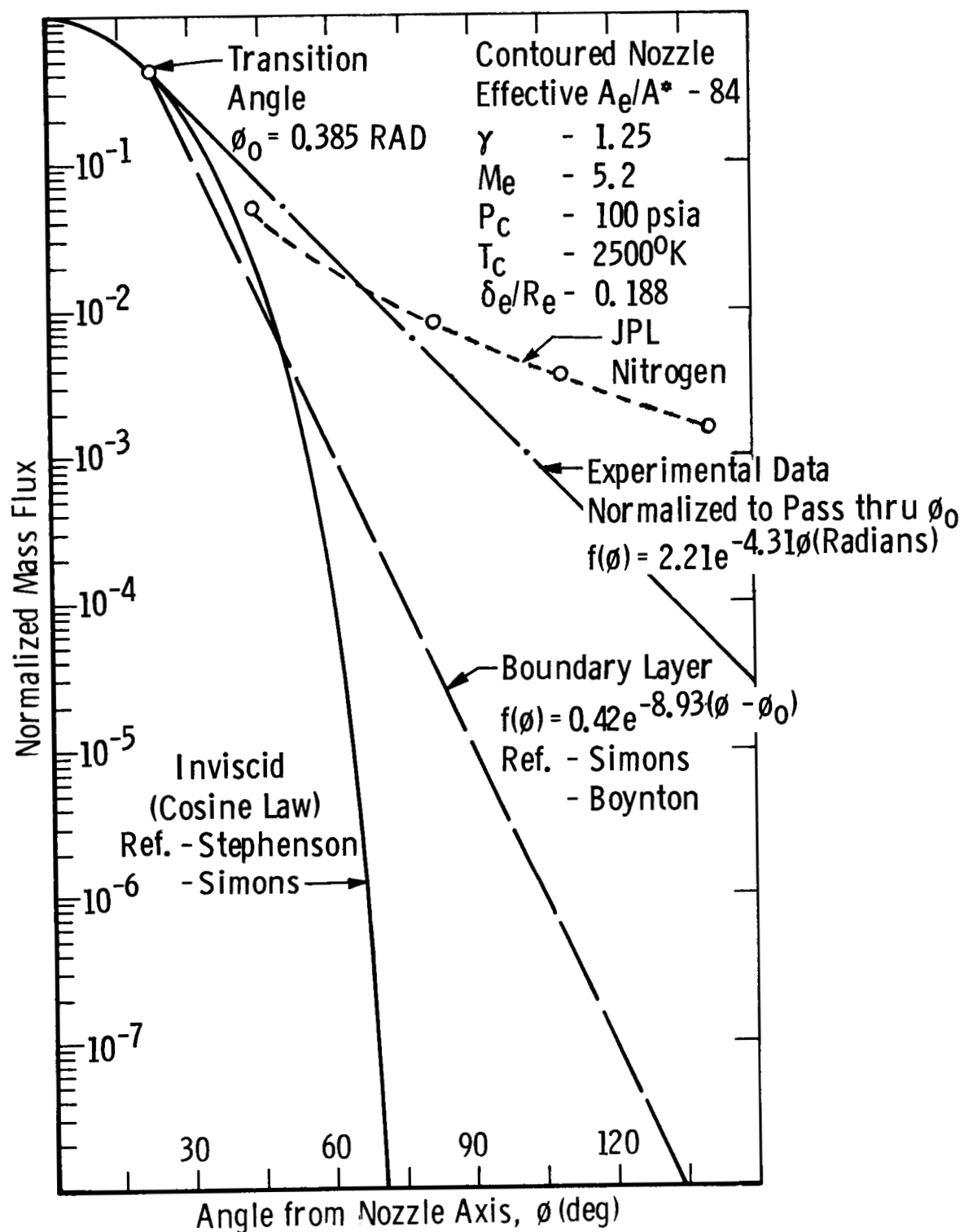
Fig. 14 Comparing Measured and Calculated Mass Flux Distributions

The figure shows a plot of Normalized Mass Flux (vertical axis, logarithmic from 10^{-7} to above 10^{-1}) versus Angle from Nozzle Axis, ϕ (deg) (horizontal axis, from 30 to 120).

Transition Angle $\phi_0 = 0.385$ RAD

Contoured Nozzle
Effective A_e/A^* - 84

γ - 1.25
M_e - 5.2
P_c - 100 psia
T_c - 2500°K
δ_e/R_e - 0.188

JPL Nitrogen

Experimental Data Normalized to Pass thru ϕ_0
$f(\phi) = 2.21e^{-4.31\phi(Radians)}$

Boundary Layer
$f(\phi) = 0.42e^{-8.93(\phi - \phi_0)}$
Ref. - Simons
- Boynton

Inviscid (Cosine Law)
Ref. - Stephenson
- Simons

too rapidly. The slope $\beta = 8.93$ for the predicted exponential curve is a factor of two higher than that for the data. One possible source for this discrepancy could be the boundary layer input conditions which were taken from similar results[24] for ideal gases expanding into vacuum. Additional analysis is required in order to resolve this discrepancy and determine if the Simons approach is adequate for plume backflow characterization.

JPL data[10] obtained at high angles for N_2 expanding through a nozzle into vacuum is also plotted in Fig. 14. For this particular case the plenum pressure was 104 psia. At large angles the JPL data are considerably higher than the bipropellant engine data.

One final observation can be made to quickly put these measurements into proper perspective. If the measured exponential curve, Eq. (3), is extrapolated down to $0°$ and up to $180°$ and integrated over the entire sphere around the nozzle, the percentage of total mass flux from the thruster reaching the backflow hemisphere is 0.5%. The total integrated mass flux is 3 gm/sec compared to a propellant flow rate of 5 gm/sec.

5.0 CONCLUSIONS

1. The cryogenic chamber provided an adequate simulation of space operating conditions and had no significant effect on the plume flow field or the mass flux collected by the QCMs.

2. Variation of engine configuration had no measureable effect on the mass flux distribution.

3. Variation of engine operating conditions, with the exception of pulse length, had no significant effect on the mass flux distribution.

4. The QCM data show a smooth exponential mass flux distribution at angles greater than 30° from the plume axis. This strongly suggests that a proper treatment of the boundary layer is required to correctly predict mass flux in the backflow region.

5. At the higher QCM temperatures (greater than $180^\circ K$) where condensation of major exhaust species is not expected, approximately 1 - 2% of the total mass flux was collected throughout the exhaust plume. These constituents, generally identified as nitrates, represent potential contaminants for spacecraft surfaces.

6. The QCM design modifications (thermally separated electronics) permitted reliable operation to temperatures as low as $25^\circ K$.

7. By far the largest uncertainty in the QCM data is attributed to uncertainty in the calibration constant. QCMs must be calibrated over the entire temperature range of operation. Field-of-view effects should be investigated.

ACKNOWLEDGMENTS

REFERENCES

1. Chirivella, J. E., "ATS-F Radiant Cooler Contamination Test in a Hydrazine Thruster Exhaust", JPL-TM-33-592 (1973).

2. Davis, L. P. and Witbracht, I. L., "Thruster Contamination Predictions for NATO III Satellite", AFRPL-TR-75-67 (1975).

3. Burch, B. A., "Effect of Contamination on Spacecraft Surfaces Exposed to Rocket Exhausts", AEDC-TR-68-23 (1968).

4. Bowman, R. L., et al, "Skylab Plume Contamination Experiments", NASA-TM-X-71474 (1973).

5. Lynch, J. T., "Quartz Crystal Microbalance (QCM) Monitor of Contamination for LES 8/9", Project Report SC-33, Lincoln Laboratory, Massachusetts Institute of Technology (1976).

6. Oeding, R. G., et al, "Space Shuttle RCS Plume Contamination Study", McDonnell Douglas Astronautics Co., MDE G5250 (1974).

7. Hoffman, R. J., et al, "Plume Contamination Effects Prediction - The CONTAM Computer Program, Version II", AFRPL-TR-73-46 (1973).

8. Davis, L. P. and Wax, S. G., "Verification of Contamination Predictions for Monopropellant Thrusters", AFRPL-TR-77-56 (1977).

9. Baerwald, R. K. and Passamaneck, R. W., "Monopropellant Exhaust Plume Contamination Measurements", AFRPL-TR-77-44 (1977).

10. Chirivella, J. E., "Hydrazine Engine Plume Contamination Mapping", AFRPL-TR-75-16 (1975).

11. Williams, W. D., et al, "Experimental Study of Monopropellant Hydrazine Thruster Exhaust", Proceedings of the 10th JANNAF Plume Technology Conference, San Diego, CA (1977).

12. Chirivella, J. E., "Molecular Flux Measurements in the Back Flow Region of a Nozzle Plume", JPL-TM-33-620 (1973).

13. Williams, W. D. and Lewis, J. W. L., "Condensation Scaling Laws for Reservoir and Nozzle Parameters and Gas Species as Determined by Laser Scattering Experiments", AFRPL-TR-76-67 (1976).

14. Spisz, E. W., et al, "Exhaust Plume and Contamination Characteristics of a Bipropellant RCS Thruster", Proceedings of the 7th JANNAF Plume Technology Conference, Huntsville, AL (1973).

15. Schoenman, L. and Schindler, R. C., "Five-Pound Bipropellant Engine", AFRPL-TR-74-51 (1974).

16. Pipes, J. G., et al, "Transmission of Infrared Materials and Condensed Gases at Cryogenic Temperatures", AEDC-TR-77-71 (1977).

17. Williams, W. D. and Lewis, J. W. L., "Rotational Temperature and Number
Density Measurements of N_2, O_2, CO, and CO_2 in a Hypersonic Flow Field
Using Laser-Raman Spectroscopy", AEDC-TR-75-37 (1975).

18. Stockbridge, C. D., in Vacuum Microbalance Techniques, K. H. Behrndt,
ed. (Plenum Press, New York, 1966), Vol 5, p. 193.

19. Roux, J. A., et al, "IR Optical Properties of Bipropellant Cryo-
contaminants", paper presented at the USAF/NASA International
Spacecraft Contamination Conference, USAF Academy, CO (1978).

20. AEDC Facilities Handbook (Tenth Edition), Arnold Engineering Develop-
ment Center (1974).

21. Schoenman, L. and Lundgreen, R. B., "AJ10-181 5 lb_f Bipropellant
Engine, Users Manual", Final Report, Contract PO TA1902G, Aerojet
Liquid Rocket Company (1976).

22. Honig, R. E. and Hook, H. O., "Vapor Pressure Data for Some Common
Gases", RCA Review, Vol XXI, 360 (September 1960).

23. Hill, J. A. F. and Draper, J. S., "Analytical Approximation for the
Flow from a Nozzle into a Vacuum", J. Spacecraft Rockets 3,
1552 (1966).

24. Stephenson, W. B., et al, "Development of an Integrated Cryogenic
Pumping System for Rocket Plume Studies", AEDC-TR-71-19 (1971).

25. Boynton, F. P., "Exhaust Plumes from Nozzles with Wall Boundary
Layers", J. Spacecraft Rockets 5, 1143 (1968).

26. Simons, G. A., "Effect of Nozzle Boundary Layers on Rocket Exhaust
Plumes", AIAA Journal 10, 1534 (1972).